

# Shallow shelf approximation as a “sliding law” in a thermomechanically coupled ice sheet model

Ed Bueler<sup>1</sup> and Jed Brown<sup>2</sup>

Received 23 October 2008; revised 15 April 2009; accepted 12 May 2009; published 31 July 2009.

[1] The shallow shelf approximation, a balance of membrane stresses for ice flow, is an effective “sliding law” for ice sheet modeling. Our use of it as a sliding law becomes a standard model for ice stream flow when the sliding velocity is large ( $100 \text{ m a}^{-1}$  and faster). Following Schoof (2006a), we describe the basal resistance as plastic till for which the yield stress is given by a Mohr-Coulomb formula. Pore water pressure is related to basal melt rate. The velocity field used in the mass continuity and conservation of energy equations is an average of velocities from the shallow shelf approximation and the nonsliding shallow ice approximation. Using this scheme, our model has realistic, time-dependent ice streams which exhibit the range of surface velocities seen in actual ice streams. We demonstrate the model at high spatial resolution (5 km grid) over multiple millenia using its implementation in the Parallel Ice Sheet Model. Numerical experiments show that the entire scheme is stable with respect to many parameter changes. Some experiments reveal significant ice stream variability in a hypothetical steady climate, with characteristic cycles on the order of 1000 years. We believe this is the first practical whole ice sheet model with a unified treatment of vertical shear stresses and membrane stresses. It is capable of high-resolution, thermomechanically coupled, multimillenia simulations of ice sheets containing ice streams.

**Citation:** Bueler, E., and J. Brown (2009), Shallow shelf approximation as a “sliding law” in a thermomechanically coupled ice sheet model, *J. Geophys. Res.*, 114, F03008, doi:10.1029/2008JF001179.

## 1. Introduction

[2] A well-known difficulty with numerical ice sheet models is their inability to model the large range of ice flow speeds observed in real ice sheets [Shepherd and Wingham, 2007; Truffer and Fahnestock, 2007; Vaughan and Arthern, 2007]. Observed surface speeds for ice flow in the Greenland ice sheet, for example, range from less than  $10 \text{ m/a}$  in large areas of the interior [compare Greve, 1997b; Joughin et al., 1997] to more than  $10 \text{ km/a}$  in three outlet glaciers [Howat et al., 2007; Joughin et al., 2004a]. Existing Greenland ice sheet models rarely report ice surface speeds in excess of  $100 \text{ m/a}$ , however, and they lack the resolution to resolve individual ice streams and outlet glaciers [Greve, 1997b, 2000; Ritz et al., 1997; Saito and Abe-Ouchi, 2005; Tarasov and Peltier, 2002].

[3] Fast grounded ice flow, in ice streams and outlet glaciers to differing degrees [Truffer and Echelmeyer, 2003], arises from some combination of sliding over a rigid or deformable mineral bed and shear deformation of the lowest layers of ice, which may intermingle with till [Clarke, 2005]. Unfortunately and fundamentally, however,

remote sensing provides no high-quality spatially distributed observations of conditions at or near the ice base with which to constrain models of fast flow. There is a triple need to improve observations, to use existing surface observations more effectively, and to improve models of ice flow and sliding.

[4] This paper approaches the modeling of fast ice stream motion pragmatically, within the high-resolution, thermomechanically coupled, time-dependent, and open source Parallel Ice Sheet Model (“PISM”; E. Bueler et al., PISM, a Parallel Ice Sheet Model: User’s Manual, 2009, available at [www.pism-docs.org](http://www.pism-docs.org)). The basal mechanical model we add here is based on a plastic till assumption and is parameterized by a spatially distributed till friction angle [Clarke, 2005; Paterson, 1994; Tulaczyk et al., 2000a]. We demonstrate that our model responds in a reasonable way to major parameter changes in till friction angle and other major parameter choices including grid refinement. In this model, ice sheet geometry, ice stream locations, and thermodynamical fields (ice temperature and effective thickness of basal water) all evolve together within a unified framework.

[5] Fast-flowing simulated ice is not useful in a model if it arises from unreasonable physics. All ice sheet models incorporate approximations. Most models, including ours, use the shallowness, namely the small depth to width ratio, of ice sheets and ice streams to simplify the equations and reduce computational cost. We recall some continuum flow models applied to ice sheets and sliding as a hierarchy in

<sup>1</sup>Department of Mathematics and Statistics, University of Alaska Fairbanks, Fairbanks, Alaska, USA.

<sup>2</sup>Versuchsanstalt für Wasserbau, Hydrologie und Glaziologie, ETH Zurich, Zurich, Switzerland.

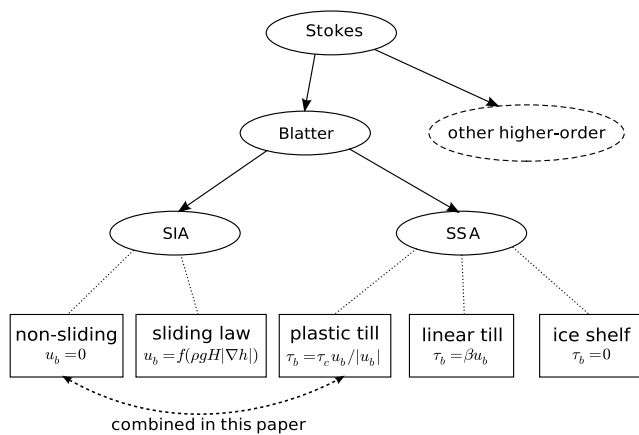


**Figure 1.** A hierarchy of ice dynamics models (ellipses) with the sliding parameterizations which have been applied to the two shallow models (boxes). Solid arrows show rigorous small-parameter shallowness arguments.

Figure 1. All the illustrated models describe ice as a slow, nonlinearly viscous, isotropic fluid, though these qualities are approximations too.

[6] The simplest and shallowest models are called the shallow ice approximation (“SIA”) [Hutter, 1983; Morland and Johnson, 1980] and the shallow shelf approximation (“SSA”) [Morland, 1987; Weis et al., 1999]. Rigorous small-parameter arguments explain how to simplify from Stokes to “higher-order models” [Blatter, 1995; Hindmarsh, 2004], and from the Blatter [1995] model to the SIA and the SSA (C. Schoof and R. Hindmarsh, Thin-film flows with wall slip: An asymptotic analysis of higher order glacier flow models, submitted to *Quarterly Journal of Mechanics and Applied Mathematics*, 2009).

[7] Thermomechanically coupled, shallow, grounded, and nonsliding ice sheet models based upon the SIA are relatively well understood [Bueler et al., 2007; Payne et al., 2000]. Large portions of actual ice sheets have bases which experience minimal sliding and have modest bed topography. For those parts the nonsliding SIA is a second-order [Fowler, 1997] theory which predicts a reasonable distribution of flow at rates which compare well to observations [e.g., Greve, 1997b].

[8] As noted, faster ice flow comes from a combination of sliding over the mineral base along with deformation of a thin till and ice layer at the base. We necessarily lump these mechanisms as “sliding” in the language of this paper, because of the lack of whole-ice-sheet-scale observational techniques necessary to distinguish them [Clarke, 2005]. Sliding applies a boundary force (stress) to the base of the ice mass, the effect of which is distributed by the stress balance. In our discussion of stress balance models below, components of the stress tensor will be separated into shear in planes parallel to the geoid (“vertical plane shear”) versus the other “membrane” stresses [Hindmarsh, 2004, 2006].

[9] The SIA has no mechanism for balancing the driving stress by membrane stresses, nor any method of incorporating the sliding stress into a stress balance at all. Nonetheless, “sliding laws” have been added to SIA models anyway [e.g., Greve, 1997b; Greve et al., 2006; Huybrechts

and de Wolde, 1999; Payne et al., 2000]. Such laws necessarily describe the velocity of the base of the ice as an explicit function of the driving stress. (The driving stress is the product of the hydrostatic pressure at the base and the surface slope [Paterson, 1994].) Furthermore, sliding is usually assumed to be insignificant when the ice base is frozen, but to “turn on” when the ice base reaches the pressure-melting temperature [e.g., Greve et al., 2006; Marshall et al., 2002; Payne et al., 2000] or to change discontinuously at sufficient depth below sea level [Huybrechts and de Wolde, 1999; Tarasov and Peltier, 2002]. Unfortunately, the SIA continuum model then propagates jump discontinuities in the horizontal velocity field to the entire ice column. This produces unbounded vertical velocities because of the incompressibility of the ice [Fowler, 2001]. These characteristics of the continuum model have the unfortunate consequence that numerical schemes for temperature or age will not converge under grid refinement, and, in fact, flow predictions from such numerical models become more unreasonable on finer grids (Appendix B).

[10] To be physically authentic, modeled sliding must, however, depend on the strength of the basal material and on the amount of liquid water present at the ice base. The former quantity (strength) is generally related to the latter (amount of water), and the amount of water is related to the ice thermodynamic state. Ice basal temperature and basal water must evolve if modeled ice streams are to exhibit the observed energy-balance-dependent behavior actually seen [Raymond, 2000; Schoof, 2004]. The coupling could include a detailed model of till deformation [Pollard and DeConto, 2008], a model of till pore void size [Tulaczyk et al., 2000b], or a distributed model for melt water conservation [Johnson and Fastook, 2002]. This paper does not yet include these process models. At least, the use of such process models requires care because they significantly increase the number of poorly constrained parameters.

[11] Instead, an effective thickness for the water stored in the till is computed by time integrating the rate of melt water production at the ice base. A negative melt rate (freeze on) is allowed. The modeled pore water pressure is a function of this effective liquid thickness. This pore water pressure is only used when computing the effective pressure on the mineral till. The Mohr-Coulomb criterion describes the yield stress of the saturated till as the product of the effective pressure on the till and the tangent of the till friction angle [Paterson, 1994]. Finally, saturated till strength (yield stress) enters as a term in a membrane stress balance, the SSA.

[12] Large ice shelves with zero till strength are well described by the SSA [MacAyeal et al., 1996; Morland, 1987; Weis et al., 1999]. Published Antarctic ice sheet models use the SSA for the force balance in ice shelves [Huybrechts, 1990; Huybrechts and de Wolde, 1999; Ritz et al., 2001]. Diagnostic models based on the “dragging ice shelf” extension of the SSA have also been applied to individual ice streams or ice stream basins [Hulbe and MacAyeal, 1999; MacAyeal, 1989]. These models have been used to recover the mechanical properties of the sliding ice base from observed surface velocities (“inverse modeling”) [Joughin et al., 2001, 2004b]. Though MacAyeal [1989] proposed a linear viscous till deformation model, the mechanical properties of the till in real ice streams and

outlet glaciers are a largely open question, with credible arguments for linear and plastic (Coulomb) models [Joughin *et al.*, 2004b; Schoof, 2006b; Tulaczyk *et al.*, 2000a, 2000b]. Power law formulations interpolate between these extremes [Schoof, 2009].

[13] Attempts have been made, including by the current authors, to incorporate ice streams into shallow whole ice sheet models by marking some map-plane points as “sheet” and some points as “stream.” In such a scheme the SIA and SSA stress balances are used for the marked points, respectively. For example, a Hudson Strait ice stream hypothesized for the Laurentide Ice Sheet in North America has been modeled by Marshall and Clarke [1997a, 1997b] using such a scheme. In attempting to apply such a scheme to the West Antarctic Ice Stream at higher resolution, however, we and others [Hulbe and MacAyeal, 1999; Ritz *et al.*, 2001] have observed an unmanageable velocity and flux matching problem at locations where sheet and stream flows meet. Furthermore the locations of stream flow must be specified in advance. There exists no obvious mechanism for evolving in time the sheet versus stream marking scheme.

[14] The current paper assumes that the till behaves as a (regularized) plastic material. This is in part because the best understood continuum model which includes the SSA stress balance uses plastic till as part of a well-posed free boundary problem for the velocity. In fact, Schoof [2006a] has recognized, in the isothermal and time-independent (diagnostic) case, that including plastic failure of the basal till under flowing ice gives emergent ice streams within a whole ice sheet system. Our inclusion of Schoof’s model into a time-dependent model is new. The locations of sliding flow are not predetermined in Schoof’s model or in our model. In our model the extent of sliding also evolves thermodynamically, through the pore water pressure mechanism sketched above.

[15] We use the SSA model as a sliding law in a thermomechanically coupled SIA model. The boundaries of the sliding regions are locations where the sliding velocities go to zero in a well-behaved way [Schoof, 2006a], so the problems described in Appendix B do not arise. The majority of the flow, by map-plane area or ice volume fraction, is by vertical plane shear according to the nonsliding SIA. There are, however, ice streams which flow partly by the SIA but mostly by additional basal sliding constrained by the SSA membrane stress balance. The ice is allowed to slide anywhere, but sliding does not occur in the majority of the basal area because the till is too strong. Though till friction angle is time independent, the actual till strength (yield stress) evolves in a thermomechanically coupled and time-dependent manner through evolution of the modeled pore water pressure.

[16] The sliding velocity field arising at a particular time from the solution of the SSA is averaged with the velocity field which solves the nonsliding SIA at that time. This is the sense in which the SSA is a sliding law. As a result, the velocity field is a weighted average of values from two published ice sheet models, namely the nonsliding SIA [Hutter, 1983] and a plastic till form of the SSA [Schoof, 2006a]. The average is weighted toward the SIA if sliding is slow and toward the SSA if sliding is fast (section 2.8).

[17] Our model is time dependent in the usual sense that ice sheet geometry evolves according to a mass continuity equation. The flow is thermomechanically coupled in the usual senses that the temperature affects the softness of the ice and there is dissipation heating from ice deformation and frictional heating from sliding.

[18] As suggested by Figure 1, our shallow hybrid stress balance is not as complete as a number of higher-order or “full Stokes” alternatives [Pattyn *et al.*, 2008]. The Stokes model is, however, a three independent variable  $(x, y, z)$  problem for the velocity field. Such a stress balance must be solved at each time step. It has currently only been solved either for thermomechanically coupled but diagnostic problems on glaciers [e.g., Zwinger *et al.*, 2007] or with geometry evolution but isothermally and again on glacier-sized problems [e.g., Pattyn *et al.*, 2008]. The stress balance for the Blatter [1995] model is likewise a three independent variable problem. It has been implemented for whole ice sheets but not at high resolution [Pattyn, 2003; Saito *et al.*, 2006]. The SSA stress balance solution used here is vertically integrated and involves only two independent variables  $(x, y)$ , a significant computational simplification.

## 2. Continuum Model

[19] Our description of the continuum model is organized into eight subsections (sections 2.1–2.8): mass continuity, flow law, conservation of energy, basal melt, SIA version of the stress balance, SSA version of the stress balance, basal mechanics, and combination of velocity fields. Notation follows Table 1.

[20] The time-independent boundary and geometry data are bed elevation  $b(x_1, x_2)$ , ice surface temperature  $T_s(x_1, x_2)$ , and accumulation rate  $M(x_1, x_2)$ . The modeled time-dependent unknowns are the ice thickness  $H(t, x_1, x_2)$ , surface elevation  $h(t, x_1, x_2)$ , basal melt rate  $S(t, x_1, x_2)$ , thickness of a melt water layer  $W(t, x_1, x_2)$ , temperature  $T(t, x_1, x_2, x_3)$ , and vector velocity  $\mathbf{U}(t, x_1, x_2, x_3)$ . The relation  $h = H + b$  holds always because only grounded ice sheets are considered here. Let  $D_{ij}$  be the strain rate tensor, that is,  $D_{ij} = (1/2)(\partial U_i/\partial x_j + \partial U_j/\partial x_i)$ . Let  $\sigma_{ij}$  be the full (Cauchy) stress tensor,  $p = -(1/3)(\sigma_{11} + \sigma_{22} + \sigma_{33})$  the pressure, and  $\tau_{ij} = \sigma_{ij} + p\delta_{ij}$  the deviatoric stress tensor.

### 2.1. Mass Continuity

[21] The upper surface  $z = h$  of the ice is a free surface. Let  $U_{h,i} = U_i(z = h)$  be the surface value of the velocity. Then, using a small slope assumption for the ice surface [Fowler, 1997],

$$\frac{\partial h}{\partial t} = M + U_{h,3} - \nabla h \cdot (U_{h,1}, U_{h,2}) \quad (1)$$

is the surface kinematical equation. (The gradient  $\nabla$ , divergence  $\nabla \cdot$ , and scalar product  $\mathbf{v} \cdot \mathbf{w}$  are always in the horizontal variables  $x_1, x_2$ .) A similar  $\nabla$  is in the horizontal variables. A similar equation applies at the base of the ice

$$0 = S + U_{b,3} - \nabla b \cdot (U_{b,1}, U_{b,2}). \quad (2)$$

[22] Define  $\mathbf{Q} = \bar{\mathbf{U}}H$ , the horizontal ice flux, where  $\bar{\mathbf{U}}$  is the vertically averaged horizontal velocity. For the

**Table 1.** Notation, Units, and Values for Constants<sup>a</sup>

Symbol	Description	SI Units	Value
$A(T^*)$	temperature-dependent factor in ice flow law; equation (5)	$\text{Pa}^{-3} \text{s}^{-1}$	
$B(T^*)$	ice hardness; $B(T^*) = A(T^*)^{-1/n}$	$\text{Pa s}^{1/3}$	
$b$	bed elevation	m	
$\beta$	dependence of melting point on depth	$\text{K m}^{-1}$	$8.66 \times 10^{-4}$
$c_i$	specific heat capacity for ice	$\text{J (kg K)}^{-1}$	2009
$D_{ij}$	strain rate tensor	$\text{s}^{-1}$	
$D_L$	depth of lithosphere thermal model (see text)	m	515
$D_{\text{SIA}}$	diffusivity associated to SIA; equation (24)	$\text{m}^2 \text{s}^{-1}$	
$\delta$	regularizing velocity for plastic till; equation (27)	$\text{m s}^{-1}$	$0.01 \text{ m a}^{-1}$
$\epsilon$	regularizing velocity for effective viscosity; equation (26)	$\text{m s}^{-1}$	$1.0 \text{ m a}^{-1}$
$f( \mathbf{v} )$	weighting function for averaging velocities; equations (21) and (22)		
$\phi$	till friction angle; equation (19)		
$G_0$	geothermal flux	$\text{W m}^{-2}$	.042
$g$	acceleration of gravity	$\text{m s}^{-2}$	9.81
$h$	ice surface elevation	m	
$H$	ice thickness	m	
$k_i$	thermal conductivity of ice	$\text{W (K m)}^{-1}$	2.10
$K_r$	thermal diffusivity of lithosphere	$\text{m}^2 \text{s}^{-1}$	$9.09 \times 10^{-7}$
$L$	latent heat of fusion for ice	$\text{J kg}^{-1}$	$3.35 \times 10^5$
$\bar{L}$	diffusion distance for melt water thickness; equation (11)	m	20 km
$L_\nu$	regularizing length for effective viscosity; equation (26)	m	$10^6$
$M$	ice equivalent surface mass balance	$\text{m s}^{-1}$	
$n$	Glen exponent in ice flow law; equation (5)		3
$\bar{\nu}$	vertically averaged (effective) viscosity in SSA; equation (14)	$\text{Pa s}$	
$\mathbf{Q}$	horizontal ice flux	$\text{m}^2 \text{s}^{-1}$	
$p$	pressure (in ice)	Pa	
$p_w$	pore water pressure in till; equation (20)	Pa	
$R$	gas constant	$\text{J (mol K)}^{-1}$	8.314
$\rho_i$	density of ice	$\text{kg m}^{-3}$	910
$S$	ice equivalent basal mass balance ( $S > 0$ is melting)	$\text{m s}^{-1}$	
$T$	absolute ice (or bedrock) temperature	K	
$T^*$	pressure-adjusted ice temperature; $T^* = T_0 - \beta(h - z)$	K	
$T_0$	melting temperature for ice	K	273.15
$T_s$	surface temperature	K	
$t$	time	s	
$\bar{t}$	diffusion time for melt water thickness; equation (11)	s	1000 years
$\tau_{b,i}$	basal shear stress applied to ice; equation (18)	Pa	
$\tau_c$	till yield stress	Pa	
$\tau_{ij}$	deviatoric stress tensor	Pa	
$\mathbf{u} = (u_i)$	horizontal velocity computed from SIA; equation (13)	$\text{m s}^{-1}$	
$\mathbf{U} = (U_i)$	three-dimensional ice velocity; note equation (21)	$\text{m s}^{-1}$	
$\bar{\mathbf{U}}$	vertically averaged horizontal velocity	$\text{m s}^{-1}$	
$\mathbf{U}_b$	basal value of the ice velocity	$\text{m s}^{-1}$	
$\mathbf{v} = (v_i)$	horizontal velocity computed from SSA; equation (17)	$\text{m s}^{-1}$	
$W$	effective thickness of basal water; equation (11)	m	
$W_0$	limit on $W$ , a basal drainage parameter	m	2.0
$x_i$	cartesian coordinates; $x_3 = z$ is positive upward	m	

<sup>a</sup>Vectors are in bold.

nonsliding SIA (section 2.5), the expression  $\mathbf{Q} = -D_{\text{SIA}} \nabla h$  also applies, where  $D_{\text{SIA}}$  is a positive diffusivity [Bueler *et al.*, 2007]. For sliding balanced by membrane stresses, a diffusivity cannot be meaningfully defined because the ice flux  $\mathbf{Q}$  is not generally parallel to  $\nabla h$ . Instead we will treat the mass continuity problem associated with basal sliding as a generic transport problem (section 3.3).

[23] Ice is an incompressible fluid, so  $D_{11} + D_{22} + D_{33} = 0$ . The equation of mass continuity

$$\frac{\partial H}{\partial t} = M - S - \nabla \cdot \mathbf{Q} \quad (3)$$

can be derived from incompressibility by using the ice surface and base kinematic equations. We will solve

equation (3) numerically to compute the ice thickness at each grid point at each time step.

[24] The vertical velocity within the ice is, by incompressibility,

$$U_3 = -S + \nabla b \cdot (\mathbf{U}_{b,1}, \mathbf{U}_{b,2}) - \int_b^{x_3} \nabla \cdot (\mathbf{U}_1, \mathbf{U}_2) d\zeta. \quad (4)$$

We have included the (ice equivalent) basal melt rate  $S$  in the vertical velocity of the ice. In particular, the basal melt rate influences the vertical advection term in conservation of energy (section 2.3). Also, we have included the contribution of the basal melt rate  $S$  to the mass continuity equation (3) [cf. Payne *et al.*, 2000]. The basal melt rate will also feed back to affect ice dynamics by influencing the till yield stress (section 2.7).



## 2.2. Flow Law for Ice

[25] Ice is modeled as a nonlinearly viscous isotropic fluid with a constitutive relation of Arrhenius-Glen-Nye form [Paterson, 1994]

$$D_{ij} = A(T^*) \tau^{n-1} \tau_{ij}, \quad (5)$$

where  $T^* = T + \beta(h - z)$  is the pressure-adjusted temperature,  $n = 3$ , and  $2\tau^2 = \tau_{ij}\tau_{ij}$  determines the second stress invariant  $\tau$  [Fowler, 1997]. This form of the flow law is used for the SIA stress balance (section 2.5). The ice softness (flow factor)  $A(T^*)$  is determined by the following formulas of Paterson and Budd [1982]:

$$A(T^*) = \begin{cases} (3.61 \times 10^{-13}) e^{-6.0 \times 10^4 / (RT^*)}, & T^* \leq 263.15 \text{ K}, \\ (1.73 \times 10^{-3}) e^{-13.9 \times 10^4 / (RT^*)}, & T^* > 263.15 \text{ K}. \end{cases}$$

There is no enhancement factor.

[26] For the SSA stress balance (section 2.6) we state the same flow law in viscosity form

$$\tau_{ij} = 2\nu(T^*, D) D_{ij}. \quad (6)$$

The nonlinear viscosity  $\nu$  satisfies  $2\nu(T^*, D) = B(T^*) D^{(1/n)-1}$  where  $2D^2 = D_{ij}D_{ij}$  and  $B(T^*) = A(T^*)^{-1/n}$  is the ice hardness.

## 2.3. Conservation of Energy

[27] We use a standard conservation of energy model for cold ice (not polythermal) [Greve, 1997a]. Shallowness, namely a small ratio  $\epsilon = [H]/[L]$  of typical ice thickness  $[H]$  to typical ice sheet width  $[L]$ , simplifies the equation so that the horizontal conduction terms drop out. This simplification occurs both in the shallowness argument that leads to the SIA [Fowler, 1997] and in the one that leads to the SSA [Weis et al., 1999]. Thus the equation

$$\rho_i c_i \left( \frac{\partial T}{\partial t} + U_1 \frac{\partial T}{\partial x_1} + U_2 \frac{\partial T}{\partial x_2} + U_3 \frac{\partial T}{\partial z} \right) = k_i \frac{\partial^2 T}{\partial z^2} + \Sigma \quad (7)$$

states conservation of energy, where  $\rho_i$ ,  $c_i$ ,  $k_i$  are constant material properties of the ice (Table 1). The term in parentheses on the left of (7) is the material derivative  $dT/dt$ .

[28] We denote by  $\Sigma$  the rate at which straining is converted to heat and becomes volumetric heating. Specifically, recalling that ice sheets are a slow flow, all work done by the driving stress of gravity is immediately deposited as heat into the ice or is used for producing melt water at the base (section 2.7). In the case of the full Stokes model [Greve, 1997a],

$$\Sigma_{FS} = \sum_{i,j=1}^3 D_{ij} \tau_{ij} = 2B(T^*) D^{(1/n)+1}. \quad (8)$$

We compute the strain heating  $\Sigma$  in equation (7) using the shallow approximations of  $\Sigma_{FS}$  described in section 2.8, however.

[29] Frictional heating occurs at the ice-lithosphere interface where the ice is sliding. The rate of heating is  $-\tau_b \cdot \mathbf{U}_b$ ,

a positive value with SI units of  $\text{J m}^{-2} \text{s}^{-1}$  [e.g., Paterson, 1994, chapter 10]. This rate, times the area of the horizontal face of a grid cell, times the length of a time step, is an amount of heat which is added at each time step to the grid cell at the ice-lithosphere interface.

[30] Lithosphere “thermal inertia” is an important physical process in the thermomechanical regulation of ice stream flow, and it is a standard part of paleo ice sheet modeling [e.g., Greve, 1997b; Ritz et al., 1997]. We track the temperature of the lithosphere through a simplified conservation of energy model which again lacks horizontal conduction terms because of shallowness

$$\frac{\partial T}{\partial t} = K_r \frac{\partial^2 T}{\partial z^2}. \quad (9)$$

Here  $K_r = 3.0 \text{ W (K m)}^{-1}$ ,  $\rho_r = 3300 \text{ kg m}^{-3}$ , and  $c_r = 1000 \text{ J (kg K)}^{-1}$ , so  $K_r = k_r / (\rho_r c_r) = 9.09 \times 10^{-7} \text{ m}^2 \text{s}^{-1}$ .

[31] Our concern with basal processes including modeled liquid water in the till requires at least a “thin” modeled lithosphere thermal layer. The thermal model extends downward a distance  $D_L = 515 \text{ m}$  into the lithosphere. For more realistic simulations, with significant climate variation over ice age cycles, a deeper layer of 2 km or more is appropriate [Ritz et al., 1997]. In the experiments for this paper, however, we observe that the (time) variability of ice stream velocity is much higher if  $D_L = 0$ , including more frequent complete halts of the flow. A thin bedrock thermal layer stabilizes the frequency of the variability. We believe that a bedrock thermal layer of at least tens of meters is needed because, as the till layer changes from a fully frozen to a partly melted state and back, it is important that the thermal “inertia” in the bedrock can exert a moderating effect.

[32] The boundary conditions for equation (7) are a surface temperature to the top of each ice column and a geothermal flux to the base of the lithosphere layer

$$T|_{(z=h)} = T_s(x_1, x_2), \quad -k \frac{\partial T}{\partial x_3} |_{(z=b-D_L)} = G_0.$$

## 2.4. Basal Melt

[33] We compute a basal melt rate and model the storage of melted water locally at the base of the ice column, as follows: If at some time step the ice in a grid cell reaches the pressure-melting temperature  $T_0^* = T_0 - \beta(h - z)$  then our model converts a small fraction of the excess heat produced during that time step to melt water which appears at the base of the ice column. This fraction depends on the height above the bed. Concretely, for a time step  $\Delta t$ , equation (7) predicts tentative temperature  $\tilde{T}(t + \Delta t)$ , which might actually be above the pressure-melting temperature. Our basal melt rate  $S$  is given by

$$S \Delta t = \frac{c_p}{L} \int_b^{b+100} \left( \tilde{T}(t + \Delta t) - T_0^* \right) \left[ 0.2 \frac{b + 100 - z}{100} \right] dz. \quad (10)$$

The unitless number in square parentheses is the fraction of the melt water produced at height  $z$  which appears as free liquid water at the base. This fraction decreases linearly

from 20% at the base to 0% at 100 meters above the base, and is zero above that. The basal melt rate  $S$  can be negative in the case where water is freezing on to the bottom of the ice column. Freeze on only occurs if stored water is available at the base; storage is addressed next.

[34] The water produced by melting of ice near the base is locally stored in till. This water is described by an effective thickness  $W$ . It is available for weakening the till mechanically and for refreezing. Its thickness  $W$  is updated by adding the basal melt rate  $S$  at each time step, but with additional spatial diffusion

$$\frac{\partial W}{\partial t} = S + K_{\text{melt}} \left( \frac{\partial^2 W}{\partial x_1^2} + \frac{\partial^2 W}{\partial x_2^2} \right), \quad (11)$$

where  $K_{\text{melt}} = \tilde{L}^2/(2\tilde{\tau}^2)$ ,  $\tilde{L} = 20$  km, and  $\tilde{\tau} = 1000$  years. That is, the melt water is produced locally in each column according to (10), but it diffuses so that a delta mass spreads to a normal distribution with standard deviation of 20 km in 1000 years. Finally,  $W$  is limited to at least zero and at most  $W_0 = 2$  meters. This upper limit forms a minimal model for basal drainage. Once the basal melt rate  $S$  and the stored basal water thickness  $W$  are computed for time  $t + \Delta t$ , all temperatures within the ice are cut off at the pressure-melting temperature  $T_0^*$ :  $T(t + \Delta t) = \min\{T_0^*, T(t + \Delta t)\}$ .

[35] Section 2.7 addresses how  $W$  is used to compute till yield stress. The connection between stored basal water and till yield stress is a critical coupling in our model.

## 2.5. SIA Version of the Stress Balance

[36] The fundamental stress balance of glaciology is the Stokes model for a slow flowing fluid [Fowler, 1997]. Here “slow” has the precise meaning that inertia can be neglected in the force (stress) balance. In this paper we combine two shallow versions of the Stokes model. One is the SIA. We use only the well-justified nonsliding version of the SIA, a non-Newtonian lubrication approximation for ice [Fowler, 1997]. The nonsliding SIA gives an ice sheet flow in which the driving force of gravity is balanced exclusively by shearing within the ice.

[37] Denoting the horizontal velocity field which solves this stress balance by  $(u_1, u_2)$ , the SIA can be written as a single equation

$$\left( \frac{\partial u_1}{\partial z}, \frac{\partial u_2}{\partial z} \right) = -2(\rho g)^n A(T^*) (h - z)^n |\nabla h|^{n-1} \nabla h. \quad (12)$$

Equation (12) computes shear strain rates  $D_{13}$ ,  $D_{23}$  from local information, in the map-plane sense. Vertical integration gives

$$(u_1, u_2) = -2(\rho g)^n |\nabla h|^{n-1} \left[ \int_b^z A(T^*) (h - \zeta)^n d\zeta \right] \nabla h. \quad (13)$$

In our model the integral in square brackets is computed numerically by the trapezoid rule on a vertical grid which is finest near the base of the ice.

[38] Throughout this paper the pressure is modeled as hydrostatic,  $p = \rho g (h - z)$ . This approximation holds in both the SIA [Fowler, 1997] and the SSA [Weis et al., 1999].

## 2.6. SSA Version of the Stress Balance

[39] When there is significant sliding at the base, the driving stress is largely balanced by membrane stresses [Hindmarsh, 2006]. “Membrane stresses”, called “longitudinal” in flowline models, are deviatoric components  $\tau_{11}$ ,  $\tau_{22}$ ,  $\tau_{12}$ . Any membrane stress balance is nonlocal because the driving stress is balanced by connection to distant ice either in the along-flow direction or at the margins of regions of fast flow. The driving stress must be fully balanced by membrane stresses in cases where there is negligible traction at the base of the ice as in an ice shelf [Morland, 1987].

[40] The simplest form of a membrane stress balance derivable from the Stokes model is the SSA. It describes a fluid membrane of variable thickness in which gravity causes spreading. When applied to ice streams the membrane also experiences traction (shear) forces on its base [MacAyeal, 1989].

[41] We denote the horizontal velocity field which solves the SSA stress balance by  $(v_1, v_2)$ . The horizontal velocity and the strain rates  $D_{11}$ ,  $D_{22}$ ,  $D_{12}$  modeled by the SSA are independent of depth. Denote vertically averaged hardness by  $\bar{B}$ , so  $\bar{B}H = \int_b^H B(T^*) dz$ . The vertically averaged viscosity is [MacAyeal, 1989]

$$\bar{\nu} = \frac{\bar{B}}{2} \left[ D_{11}^2 + D_{22}^2 + D_{11}D_{22} + \frac{1}{4}(D_{12} + D_{21})^2 \right]^{\frac{1-n}{2n}}. \quad (14)$$

Following Morland [1987] and Schoof [2006a], we also define a vertically integrated stress tensor

$$T_{ij} = 2\bar{\nu}H (D_{ij} + (D_{11} + D_{22})\delta_{ij}) \quad (15)$$

for  $i, j = 1, 2$ . The trace  $T_{11} + T_{22}$  is not generally zero so the membrane flow is conceptually “compressible” in the map plane. In fact  $T_{11} + T_{22} = (2\bar{\nu}H)(-3D_{33})$  so a negative value for  $T_{11} + T_{22}$  is a map-plane “pressure” causing an upward strain rate  $D_{33} = \partial v_3/\partial z > 0$ .

[42] Let  $(\tau_{b,1}, \tau_{b,2})$  be the basal shear stress components applied to the base of the ice (modeled in section 2.7). The SSA is the pair of equations

$$\frac{\partial T_{i1}}{\partial x_1} + \frac{\partial T_{i2}}{\partial x_2} + \tau_{b,i} = \rho g H \frac{\partial h}{\partial x_i} \quad (16)$$

for  $i = 1, 2$  [Schoof, 2006a]. A slightly more concrete form is [MacAyeal, 1989; Weis et al., 1999]

$$\begin{aligned} \frac{\partial}{\partial x_1} \left[ 2\bar{\nu}H \left( 2\frac{\partial v_1}{\partial x_1} + \frac{\partial v_2}{\partial x_2} \right) \right] + \frac{\partial}{\partial x_2} \left[ \bar{\nu}H \left( \frac{\partial v_1}{\partial x_2} + \frac{\partial v_2}{\partial x_1} \right) \right] \\ + \tau_{b,1} = \rho g H \frac{\partial h}{\partial x_1}, \\ \frac{\partial}{\partial x_1} \left[ \bar{\nu}H \left( \frac{\partial v_1}{\partial x_2} + \frac{\partial v_2}{\partial x_1} \right) \right] + \frac{\partial}{\partial x_2} \left[ 2\bar{\nu}H \left( \frac{\partial v_1}{\partial x_1} + 2\frac{\partial v_2}{\partial x_2} \right) \right] \\ + \tau_{b,2} = \rho g H \frac{\partial h}{\partial x_2}. \end{aligned} \quad (17)$$

[43] Because our emphasis is on a novel interpretation of the SSA as a sliding law, we supply a heuristic. Equation (17) splits the driving stress

$$\left( \begin{array}{c} \text{membrane stresses} \\ \text{held by viscous} \\ \text{deformation} \end{array} \right) + \left( \begin{array}{c} \text{stress held} \\ \text{at base by} \\ \text{till strength} \end{array} \right) = \left( \begin{array}{c} \text{driving} \\ \text{stress} \end{array} \right).$$

On one extreme, ice shelves have zero basal stress so the leftmost term fully supports the driving stress. On the other extreme, the nonsliding case, none of the driving stress is held by the membrane strain rates. In the latter case the SSA predicts no flow so we propose that the SIA should “take over” and predict flow by shear in vertical planes.

[44] We will solve equations (17) numerically at each time step to determine velocities  $v_i$  from evolving geometry and temperature. These equations are elliptic. More precisely, these equations can be derived from a well-posed variational problem for a convex and bounded below functional [Schoof, 2006a, equation (3.13)]. Also, however, we will couple the SSA with equations (3) and (7). Such a time-evolving coupled system is not yet known to be mathematically well posed, though we observe no behavior suggesting the contrary.

[45] To provide stress boundary conditions at the margins of the ice sheet, [Schoof, 2006a] describes the entire ice sheet as surrounded by ice shelves. For the strictly grounded theory of the current work we have an ice sheet surrounded by ice-free land. Therefore, to maintain ellipticity of the SSA we extend an entirely notional sheet to the whole rectangular computational domain, but only for the SSA computation. Specifically, we make the value for  $\bar{\nu}H$  positive everywhere by setting, where there is no ice,  $\bar{\nu}H = 4.7 \times 10^{16}$  m Pa s. (This corresponds to, for example, a thickness of 50 m, a uniform strain rate of 100 m/a per 100 km, and a vertically integrated hardness of  $\bar{B} = 1.9 \times 10^8$  Pa s<sup>1/3</sup>. The value for  $\bar{B}$  is typical of the Ross ice shelf [MacAyeal et al., 1996].) Where there is no ice the value of yield stress  $\tau_c$  is set to  $10^6$  Pa. As a result of these choices the notional extension experiences very minimal sliding at any distance beyond one grid cell width from the nearest positive thickness ice sheet. We also impose periodic boundary conditions at the edge of the computational domain, though this is of minimal significance because no sliding occurs at that distance from the ice sheet.

## 2.7. Basal Mechanics

[46] We follow Schoof [2006a] and assume that the basal shear stress has plastic form

$$\tau_{b,i} = -\tau_c \frac{v_i}{(v_1^2 + v_2^2)^{1/2}} \quad (18)$$

for  $i = 1, 2$ , where  $\tau_c$  is a positive scalar yield stress [Paterson, 1994]. Conceptually, because the till is assumed to be plastic, it supports applied stress without deformation until the applied stress equals the yield stress, at which point some amount of deformation occurs, as controlled by the stress balance equations. In our model  $\tau_c$  necessarily represents the yield stress of the aggregate material at the

base of an ice sheet, a poorly observed combination of liquid water, ice, and granular till [Clarke, 2005].

[47] In fact  $\tau_{b,i}$  is only literally given by equation (18) in map-plane locations where sliding is occurring. In locations where no sliding occurs, the driving stress on the right side of (17) is equal to the left side in the sense that the basal stress equals the driving stress. Where the base is not sliding, no division by zero occurs in the mathematically precise form of equations (17) because the problem is posed as minimizing a functional involving no division. At its minimum the functional fails to have a well-defined gradient, however [Schoof, 2006a].

[48] In our thermomechanically coupled model, the value of the till yield stress is partly determined by the availability of basal water. The Mohr-Coulomb model for the yield stress of saturated till is [Paterson, 1994, chapter 8]

$$\tau_c = c_0 + (\tan \phi) (\rho g H - p_w). \quad (19)$$

Here  $c_0$  is the till cohesion,  $p_w$  is the pore water pressure (estimated below), and  $\phi$  is a “till friction angle,” a strength parameter for the till [Clarke, 2005]. We take  $c_0 = 0$  for simplicity. (Experiments give only minimal constraints on a better representative value, other than to suggest it is small compared to typical yield stresses in ice streams [Tulaczyk et al., 2000b].) The factor  $\rho g H - p_w$  is the effective pressure of the overlying ice on the mineral portion of the saturated till. The till is weakened by the presence of pressurized liquid water.

[49] Recall that we model an effective thickness  $W$  of stored liquid water at the base of the ice column. This liquid water is mixed with the solid part of the till. The thickness  $W$  is used to estimate the pore water pressure

$$p_w = 0.95 (\rho g H) \left( \frac{W}{W_0} \right), \quad (20)$$

where  $W_0 = 2$  m. As noted earlier,  $0 \leq W \leq 2$  m. Thus we model the pore water pressure locally as at most a fixed fraction (95%) of the ice overburden pressure  $\rho g H$ . When the base is frozen we have  $W = 0$ , so  $p_w = 0$  and the till is strong. With a till friction angle  $\phi = 15^\circ$  and fully saturated till, the yield stress  $\tau_c$  is 1.3% of overburden.

## 2.8. Combining the Velocities

[50] The use of an SSA result as the sliding velocity in an SIA model, the most novel aspect of our model, means combining the velocities computed by SIA and SSA to get the velocity used in mass continuity and conservation of energy. Recall that  $\mathbf{u} = (u_1, u_2)$  is the SIA velocity (section 2.5) and  $\mathbf{v} = (v_1, v_2)$  is the SSA velocity (section 2.6). We compute the combined horizontal velocity  $\mathbf{U} = (U_1, U_2)$  by

$$\mathbf{U} = f(|\mathbf{v}|) \mathbf{u} + (1 - f(|\mathbf{v}|)) \mathbf{v}, \quad (21)$$

with  $|\mathbf{v}|^2 = v_1^2 + v_2^2$  and

$$f(|\mathbf{v}|) = 1 - \frac{2}{\pi} \arctan \left( \frac{|\mathbf{v}|^2}{100^2} \right). \quad (22)$$

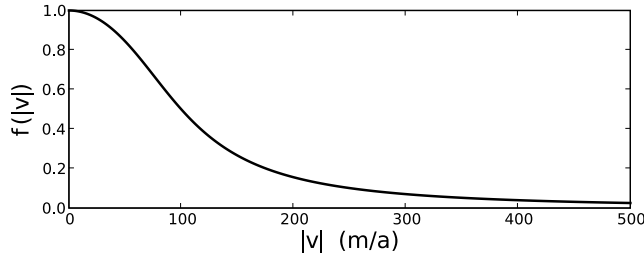


**Figure 2.** Weighting  $f(|\mathbf{v}|)$  in equation (21) versus sliding speed  $|\mathbf{v}|$ .

The weighting function  $f$  has values between zero and one. See Figure 2. It satisfies the general requirements of smoothness, monotone decrease,  $f(|\mathbf{v}|) \sim 1$  for  $|\mathbf{v}|$  small, and  $f(|\mathbf{v}|) \sim 0$  for  $|\mathbf{v}|$  large (e.g.,  $|\mathbf{v}| \gg 100$  m/a). Other choices satisfying these requirements are possible. Comparison of trusted Stokes model results to those from our model is a method for choosing an optimal weighting  $f(|\mathbf{v}|)$ .

[51] It follows from equations (21) and (13) that

$$\mathbf{Q} = -f(|\mathbf{v}|)D_{\text{SIA}}\nabla h + (1 - f(|\mathbf{v}|))\mathbf{v}H, \quad (23)$$

where

$$D_{\text{SIA}} = 2(\rho g)^n |\nabla h|^{n-1} \int_b^h A(T^*) (h - z)^{n+1} dz \quad (24)$$

is the positive diffusivity associated to the thermomechanical SIA [Bueler *et al.*, 2007, and references therein]. Note that the flux is a linear combination of a vector pointing down the surface slope and a vector determined through the SSA stress balance. Only the former part of the flux is automatically diffusive for mass continuity equation (3) [cf. Pattyn, 2003]. We address the numerical approximation of  $\mathbf{Q}$  and a time stepping scheme for equation (3) in section 3.3.

[52] Equation (8) gives the strain heating rate  $\Sigma_{\text{FS}}$  applicable to a full Stokes model. We approximate  $\Sigma_{\text{FS}}$  by a shallow quantity  $\Sigma$ . Though strain rates for  $\mathbf{u}$  and  $\mathbf{v}$  do not sum in a simple way to yield the combined strain rates  $D_{ij}$  for  $\mathbf{U}$ , we propose an approximate method for computing  $\Sigma$  in pieces. Denoting  $D(\mathbf{u})_{ij} = (1/2) (\partial u_i / \partial x_j + \partial u_j / \partial x_i)$  and  $D(\mathbf{v})_{ij} = (1/2) (\partial v_i / \partial x_j + \partial v_j / \partial x_i)$ ,

$$D_{ij} \approx f(|\mathbf{v}|)D(\mathbf{u})_{ij} + (1 - f(|\mathbf{v}|))D(\mathbf{v})_{ij}. \quad (25)$$

The SIA says that each of  $D(\mathbf{u})_{11}$ ,  $D(\mathbf{u})_{12}$ ,  $D(\mathbf{u})_{21}$ ,  $D(\mathbf{u})_{22}$  are negligible, whereas  $D(\mathbf{v})_{13}$ ,  $D(\mathbf{v})_{31}$ ,  $D(\mathbf{v})_{23}$ ,  $D(\mathbf{v})_{32}$  are all negligible in the SSA. Thus equation (25) can be rewritten

$$(D_{ij}) \approx f(|\mathbf{v}|) \begin{pmatrix} 0 & 0 & D(\mathbf{u})_{13} \\ & 0 & D(\mathbf{u})_{23} \\ & & 0 \end{pmatrix} + (1 - f(|\mathbf{v}|)) \begin{pmatrix} D(\mathbf{v})_{11} & D(\mathbf{v})_{12} & 0 \\ & D(\mathbf{v})_{22} & 0 \\ & & D(\mathbf{v})_{33} \end{pmatrix}.$$

Only entries on and above the diagonal need be displayed because of symmetry. It follows from (25) that

$$D^2 = f(|\mathbf{v}|)^2 (D(\mathbf{u})_{13}^2 + D(\mathbf{u})_{23}^2) + (1 - f(|\mathbf{v}|))^2 D(\mathbf{v})^2,$$

where  $D(\mathbf{v})^2 = D(\mathbf{v})_{11}^2 + D(\mathbf{v})_{22}^2 + D(\mathbf{v})_{12}^2 + D(\mathbf{v})_{11}D(\mathbf{v})_{22}$ . This yields a computable approximation of  $\Sigma_{\text{FS}} = 2 B(T^*) D^{(1+n)/n}$ , in terms of quantities available in the SIA and SSA stress balance computations.

### 3. Numerics and Verification

[53] Each part of the continuum model of section 2 is numerically approximated in PISM, an open source project ([www.pism-docs.org](http://www.pism-docs.org)). The numerical schemes used in PISM for the time-dependent, thermomechanically coupled, nonsliding SIA are described in Appendix A of Bueler *et al.* [2007]. In this section we describe those additional schemes which were used to produce results for this paper.

[54] All PISM numerical schemes share these properties:

[55] 1. They use finite difference approximations on a regular, rectangular grid in horizontal variables  $x_1, x_2$ .

[56] 2. They do not use a rescaling of the vertical axis [e.g., Janssen, 1977], but instead model the ice surface as a boundary between ice and air within the computational grid.

[57] 3. Time stepping is adaptive. Stability conditions appropriate to each explicit or semi-implicit time stepping numerical scheme are combined to give a next time step on the basis of the current geometry, velocity, and temperature fields.

[58] 4. PETSc, the Portable, Extensible Toolkit for Scientific computation [Balay *et al.*, 2006], is used to manage interprocess communication and the parallel, iterative solution of linear systems.

#### 3.1. Approximation of the SSA

[59] Equations (17) are nonlinear in the velocities  $v_i$ . Therefore we solve them through an iteration in which the values of the velocities from the previous time step are used to compute an initial estimate of the vertically integrated effective viscosity  $\bar{\nu}^{[0]}$ . The iteration then solves the linearized form of equation (17) to compute new velocities and updated viscosity  $\bar{\nu}^{[k]}$  with each iteration. The final values  $\mathbf{v}$  from this iteration are the “SSA velocities”. Such an iteration has been widely used to solve the diagnostic problem of computing the flow velocity in ice shelves [MacAyeal *et al.*, 1996]. Appendix A details the PISM parallel implementation.

[60] We regularize equations (14) and (18) to avoid divisions by zero. In fact, we must regularize the problem to even think of it as a system of partial differential equations, because otherwise the correct formulation of the problem is a necessarily weaker form, a variational inequality. Following Schoof [2006a], we introduce both an ice viscosity regularization and a till plasticity regularization. For the former, we replace equation (14) by

$$\bar{\nu}^\epsilon = \frac{\bar{B}}{2} \left[ \frac{\epsilon^2}{L_\nu^2} + D_{11}^2 + D_{22}^2 + D_{11}D_{22} + \frac{1}{4}(D_{12} + D_{21})^2 \right]^{\frac{1-n}{2n}}, \quad (26)$$



**Table 2.** Constants for the Exact SSA Solution<sup>a</sup>

Symbol	Meaning	Value
$B$	ice hardness	$3.7 \times 10^8 \text{ Pa s}^{1/3}$
$f$	scale for till yield stress	17.854 kPa
$h_0$	constant ice thickness	2000 m
$L$	half width of weak till	40 km
$m$	power	10
$\tan\theta$	bed slope	0.001

<sup>a</sup>Equation 4.3 of Schoof [2006a]. Values of  $B, f$  are from that source.

where  $\epsilon$  has units of velocity and  $L_\nu$  is a characteristic horizontal length scale for the membrane stresses. Our values  $\epsilon = 1 \text{ m/a}$  and  $L_\nu = 1000 \text{ km}$  give  $\epsilon/L_\nu \approx 3 \times 10^{-14} \text{ s}^{-1}$ , a strain rate which should be compared to the typical membrane strain rates in a ice stream or shelf. These typical rates are of order 100 m/a per 100 km, about  $3 \times 10^{-11} \text{ s}^{-1}$ , in the Siple Coast ice streams [MacAyeal, 1989] or the Ross ice shelf [MacAyeal et al., 1996]. Because of the squares in equation (26), for large parts of the sliding domain there is a  $10^6$  difference in magnitudes between the regularizing constant  $(\epsilon/L_\nu)^2$  and the sum of the other quantities in square brackets.

[61] For the plastic regularization we modify equation (18) by choosing a small velocity  $\delta = 0.01 \text{ m/a}$  and defining

$$\tau_{b,i}^\delta = -\tau_c \frac{v_i}{(\delta^2 + v_1^2 + v_2^2)^{1/2}}. \quad (27)$$

This regularization is only significant at or near locations where there is no sliding in the perfectly plastic model. Described another way, we have made the till linearly viscous  $\tau_{b,i} = -\beta v_i$ , with a very large coefficient  $\beta = \tau_c \delta^{-1}$ , when sliding velocities are of order  $\delta$  or smaller. Thus the ice experiences slight sliding even where the till would not fail in the perfectly plastic limit. It follows from equation (19) that this sliding is of order  $\delta$  where the base is melted but not yielding, and about  $10^{-2}\delta$  where the base is frozen and not yielding.

[62] In the context of a higher-order Blatter [1995] model, Schoof [2009] has recently shown that the ice flow velocity which results from the plasticity regularized equations converges to the purely plastic result. We expect that a similar result applies in our vertically integrated, thermomechanically coupled, and geometry-evolving case.

### 3.2. Verification of the SSA Numerics

[63] We use an existing exact solution for primary verification of our numerical approximation of the “diagnostic,” isothermal, plastic till SSA. “Verification” is used here as in computational fluid dynamics [Wesseling, 2001] to mean the comparison of numerical results to exact predictions of the continuum model.

[64] The exact solution we use appears in section 4 of Schoof [2006a], but it essentially arises in the analysis by Raymond [2000] as well. Parameters and notation for the exact solution are in Table 2. Because of translational symmetry in the downstream direction, the SSA with plastic till reduces to a one variable problem in the cross-stream coordinate  $y$ . The solution is a formula  $v(y)$  for the velocity which solves a free boundary problem describing a single

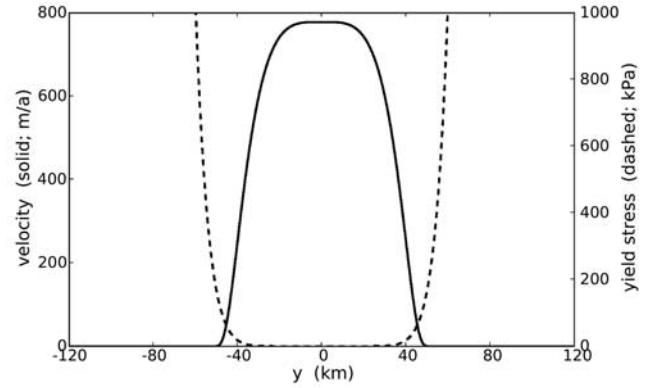


**Figure 3.** Solid curve is the ice stream velocity  $v(y)$  in the down slope direction in the exact SSA solution. Dashed curve is the till yield stress  $\tau_c(y)$ . As described in the text, the region of sliding is not predetermined.

ice stream with given till yield stress values  $\tau_c(y)$ . Because this is a free boundary problem, the width of the sliding ice stream is found simultaneously with the velocity profile  $v(y)$ . Note that the thickness, bed slope, and surface slope are all constant. We use the particular instance illustrated in Figure 3; it is called “Test I” in PISM.

[65] Our goal is to measure how well the finite difference scheme, described in Appendix A, solves this free boundary problem. Using a refinement path with  $\Delta y$  decreasing from 5 km to 40 m, the maximum and average numerical errors in velocity decay as shown in Figure 4. The numerical error at grid point  $k$  is  $|v_{\text{num}}(y_k) - v_{\text{exact}}(y_k)|$ . The maximum of these pointwise errors converges rapidly down to a level of less than  $10^{-1} \text{ m/a}$  as the grid is refined. For comparison, the exact maximum velocity is 777.5 m/a. The average error is about three times smaller than the maximum error. As shown in Figure 4, for “rough” grids with  $160 \text{ m} \leq \Delta y \leq 5 \text{ km}$  the errors decay at almost the optimal  $O(\Delta y^2)$  rate for such finite difference schemes [Morton and Mayers, 2005].

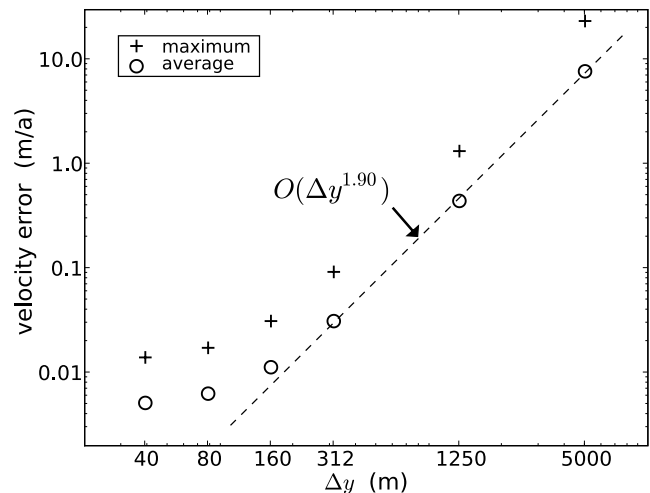


**Figure 4.** Numerical errors in along-flow velocity for the exact SSA solution shown in Figure 3. See text for convergence rate.

For the finest two grids in Figure 4 the errors are significantly influenced by the viscosity iteration relative tolerance. This tolerance has been set to  $5 \times 10^{-7}$  and the linear iteration (Krylov solver) relative tolerance to  $10^{-12}$  for these verification experiments.

[66] With regard to this SSA free boundary problem, Schoof [2006a] also demonstrates that for any aspect ratio that could conceivably be regarded as “shallow,” such as depth to width ratios of 0.1 or smaller, the velocity predictions of the SSA are very close to those of the full Stokes equations.

### 3.3. Approximation of Mass Continuity

[67] The mass continuity equation (3) is only strictly diffusive if the vertically integrated flux  $\mathbf{Q}$  is exactly in the downslope direction at all times and all locations on the ice sheet. This feature is automatic for SIA-only models, but there is no reason to expect this to be true for real ice sheets. Ice sheet flow can be expected to be diffusive at near-steady conditions and at scales of several ice thicknesses, but membrane-stress-resolving, transient-resolving, fine grid numerical schemes must assume some significant velocity components in cross-slope directions. For instance, in ice streams with minimal bed topography and low surface slope it is likely that the flow direction is controlled significantly by membrane forces including side drag and forces from margin changes and grounding line movement. A numerical scheme which treats flux as diffusive, under these conditions, risks solving an increasingly ill-posed problem as the flux deviates from downslope and as the grid reduces below a single ice thickness.

[68] In our model, flux from the SIA velocity is treated as diffusive and flux from the SSA velocity is treated as generic transport, in solving the mass continuity equation. Recalling equation (23), it follows that equation (3) can be written

$$\frac{\partial H}{\partial t} = \nabla \cdot (\tilde{D} \nabla h) - \tilde{\mathbf{v}} \cdot \nabla H - (\nabla \cdot \tilde{\mathbf{v}})H + (M - S), \quad (28)$$

where  $\tilde{D} = f(|\mathbf{v}|) D_{\text{SIA}}$  is a positive scalar and  $\tilde{\mathbf{v}} = (1 - f(|\mathbf{v}|))\mathbf{v}$ . Temporarily ignoring the distinction between  $H$  and  $h$ , equation (28) has diffusion, advection, reaction, and source terms on the right side (in that order).

[69] Our numerical approach to equation (28) is to use the simplest explicit finite difference method which is conditionally stable and consistent [Morton and Mayers, 2005]. Though we describe the scheme next as though there were only one horizontal variable  $x$ , recovery of the  $(x_1, x_2)$  form is straightforward. We will use  $m$  in the superscript to denote time step  $t^m$  and  $j$  in the subscript to denote horizontal grid point  $x_j$ . Also suppressing the superscript  $m$  on the right because all terms are evaluated at  $t^m$  (i.e., explicitly), the scheme for (28) is

$$\begin{aligned} \frac{H_j^{m+1} - H_j^m}{\Delta t} = & \frac{\tilde{D}_{j+1/2}(h_{j+1} - h_j) - \tilde{D}_{j-1/2}(h_j - h_{j-1})}{\Delta x^2} \\ & - \tilde{v}_j \frac{Up(H|\tilde{v}_j)}{\Delta x} - \left( \frac{\tilde{v}_{j+1} - \tilde{v}_{j-1}}{2\Delta x} \right) H_j + (M_j - S_j) \end{aligned} \quad (29)$$

The weighted diffusivity  $\tilde{D}_{j+1/2}$  is computed by the Mahaffy [1976] scheme as given by Bueler *et al.* [2007]. Our upwind differencing notation is  $Up(H|\tilde{v}_j) = \tilde{v}_j(H_j - H_{j-1})$  if  $\tilde{v}_j \geq 0$  while  $Up(H|\tilde{v}_j) = \tilde{v}_j(H_{j+1} - H_j)$  if  $\tilde{v}_j < 0$ . Scheme (29) is conditionally stable. A condition applies to the explicit diffusion scheme:  $(\max_j \tilde{D}_{j+1/2}^m) \Delta t < 0.5 \Delta x^2$  [Morton and Mayers, 2005, chapter 2]. The CFL condition for the upwind scheme applies:  $(\max_j \tilde{v}_j^m) \Delta t < \Delta x$  [chapter 4 Morton and Mayers, 2005]. We adaptively take  $\Delta t$  to be the largest time step which satisfies both of these conditions at every point on the grid. Though the mass continuity equation is strongly nonlinear, stability follows because the maximum principle applies [Morton and Mayers, 2005, pp. 16–18, 36–38, 50–51, and 94–96]. There is an additional condition for the stability of the conservation of energy scheme [Bueler *et al.*, 2007], and it is also included in the adaptive time stepping scheme.

## 4. Experiments

[70] The model described above is not applied to a real ice sheet in this paper, but it is being applied to the whole Greenland ice sheet (E. Bueler *et al.*, manuscript in preparation, 2009). Here we examine how the modeled flow speed and ice sheet volume depend on certain parameters. We use four experiments which explore a part of the parameter space. We study grid refinement. These experiments demonstrate the stability of the model with respect to parameter changes.

[71] All experiments use a  $1500 \times 1500$  km computational domain with equal spacing along the two horizontal axes. (The grid spacing is an adjustable parameter.) We use an unequally spaced vertical grid in the ice and air above, up to elevation 5000 m. The spacing increases from 12.9 m at the bed to 87.1 m at the top. The vertical grid in bedrock has forty equal 12.9 m grid spaces.

[72] Each of the four experiments starts from the same circular ice sheet which is the initial state. This initial state is very similar to the steady state (200 ka state) of experiment A in EISMINT II [Payne *et al.*, 2000], which is denoted “EISIIA.” The net surface mass balance and surface temperature maps are all exactly as in EISIIA. As in EISIIA, our initial state comes from a model run using only the nonsliding, thermomechanically coupled SIA. Two differences are that ours includes a bedrock thermal model (equation (9)) and modeled basal water (equation (11)). The basal melt rate is computed by equation (10). Unlike in EISIIA, the basal melt rate is included in the mass continuity and vertical velocity (equations (3) and (4), respectively). Our initial state is on a 10 km horizontal grid, versus 25 km for EISIIA.

[73] As a result, our numerically computed initial state has radius about 575 km, center thickness 3708.75 m, center (absolute) temperature at the ice base 256.24 K, and volume  $2.208 \times 10^6$  km<sup>3</sup>. Figure 5 shows the thickness and the extent of melted base.

[74] This initial ice sheet does not come from a sliding model, but it is “ready to slide” in locations where the till yield stress  $\tau_c$  is sufficiently low. Note that if the till friction angle were set to a large value everywhere (e.g., 15 or greater), then our model reduces to the nonsliding thermomechanically coupled SIA with no sliding. On the other

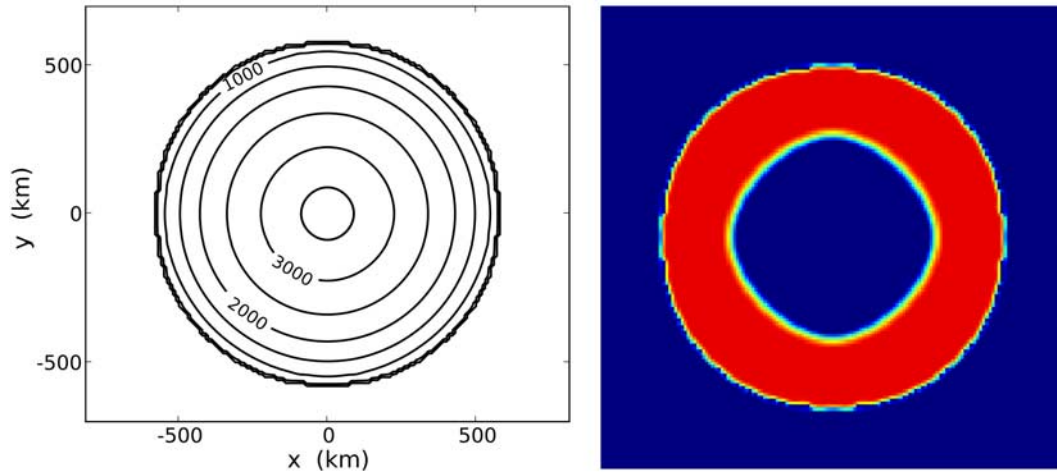


**Figure 5.** (left) Ice thickness and (right) basal water layer effective thickness  $W$  for the initial state. Water thickness  $W$  ranges from 0 (blue) to 2 m (red). The central blue area has frozen base and so  $W = 0$ . Figure 5 (right) shows a  $1500 \times 1500$  km square region. Figures 6, 8, 9, 18, and 19 show the same region.

hand, if the till friction angle were set everywhere to a sufficiently weak value (e.g.,  $5^\circ$ ) then the sheet would slide in all radial directions. Our four experiments are in between these extremes. Each experiment includes a map of till friction angle  $\phi$  with weak strips. Under most of the sheet  $\phi = 15^\circ$ , while in the weak strips we set  $\phi = 5^\circ$ , except in experiment P4 which explores this till parameter. Most experiments start from the above initial state and run for 5000 model years. One run, experiment P1 on a 10 km grid, is extended to 100 model ka. See Table 3.

[75] The spatial distribution of weak till for three of the four experiments is shown in Figure 6. Experiment P1 has four weak till strips with widths 30, 50, 70, and 100 km, aligned with the cardinal directions. The cross-stream profiles of till friction angle  $\phi$  for the four strips are shown in Figure 7. Experiment P2 has three weak till strips each with width 70 km, but oriented at  $0^\circ$ ,  $10^\circ$ , and  $45^\circ$  relative to the closest cardinal grid direction. The goal of this experiment is to determine to what degree the grid alignment of the weak strip affects model outcome. Experiments P3 and P4 each have four weak strips in the cardinal directions with identical widths of 70 km. Experiment P3 has weak till strip friction angle  $5^\circ$  like experiment P1, with cross-stream profile exactly as shown in the 70 km case in Figure 7, but there is differing bed slope in the four streams. We use the “trough” bed topography from EISMINT II experiment I, but with total elevation drops of 0, 500, 1000, and 2000 m in the 650 km length of the troughs, giving slopes of 0, 0.077, 0.154, and 0.308 percent, respectively. Finally, experiment P4 has different values for the downstream value of  $\phi$ . “Downstream” starts 400 km from the beginning of the weak strip. The different strips have downstream  $\phi$  values  $2^\circ$ ,  $3^\circ$ ,  $8^\circ$ , and  $10^\circ$ , respectively, while the upstream value is  $5^\circ$  for all strips.

[76] All experiments are grounded ice sheets without calving fronts. The combined SIA-SSA model in this paper is applied at all points, including those at the margin. We have not analyzed the asymptotic shape of the resulting grounded margin for the combined model. The margin

shape arising from the isothermal and thermomechanically coupled nonsliding SIA models is analyzed by *Bueler et al.* [2005, 2007], while numerical scheme improvements for SIA margins are given by *Saito et al.* [2007], but these results do not apply directly to our case.

[77] In preparation for section 5, Figure 8 illustrates the sense in which the initial state is “ready to slide.” In Figure 8 we compare the magnitude of the basal driving stress  $\rho g H |\nabla h|$  to the till yield stress computed from equation (19), for the till friction angle map of experiment P1. We see that the driving stress exceeds the yield stress only in the portions of the strips where the base has stored melt water; compare Figure 5. The frozen parts of the weak till strips, though they have till friction angle  $\phi = 5^\circ$ , actually have large yield stresses as a consequence of equation (19). The regions where the driving stress exceeds the yield stress are expected to slide, although the sliding velocity is controlled through the membrane stress balance by connections to nonsliding parts. Because the difference between driving and yield stress is large within the downstream portions of the weak strips, strain rates are initially large and the sliding rapid.

## 5. Results

[78] The results in this paper can be reproduced by running a script included in the PISM source code distribution. The combined time of all of our results is roughly

**Table 3.** Parameter Studies<sup>a</sup>

Name	Parameter Explored	Comments
P1	width of weak till strip	10 km grid run extended to 100 ka
P2	orientation of weak till strip	only three weak till strips
P3	bed slope	
P4	strength of downstream till	

<sup>a</sup>Each experiment runs for 5000 model years on grids of 15, 10, 7.5, and 5 km spacing, starting from the same initial state.

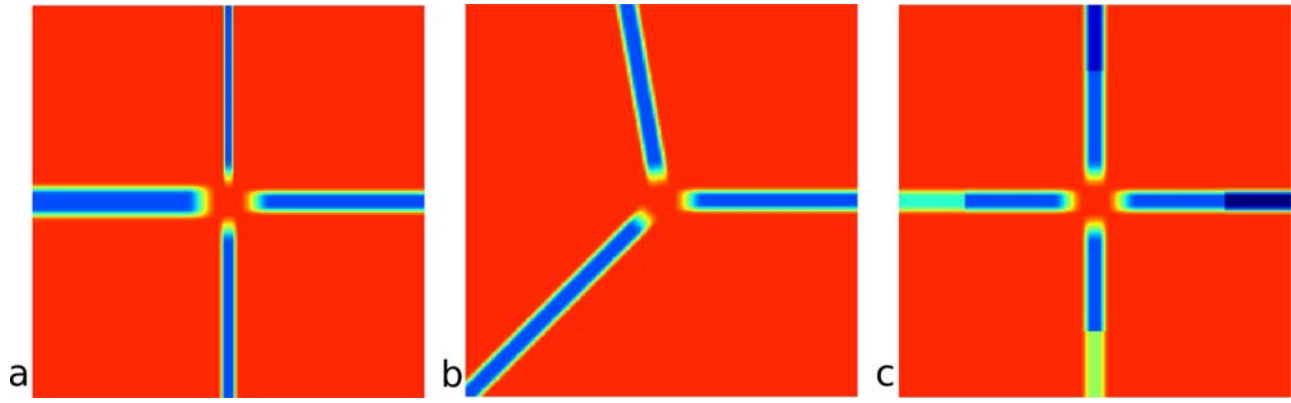


**Figure 6.** Maps of till friction angle  $\phi(x, y)$  for experiments (a) P1, (b) P2, and (c) P4. Red is 15. Blue in weak strips in Figures 6a and 6b is  $5^\circ$ , also in upstream parts of weak strips in Figure 6c. See text for downstream  $\phi$  values in experiment P4 and for the description of experiment P3.

4600 processor hours on a mix of 2.3 GHz quad core Xeon and 2.6 GHz dual core AMD Opteron processors. Runs on 5 km grids used 128 processors simultaneously.

### 5.1. Parameter Dependence

[79] A basic way to illustrate and compare flow is to show the surface velocity at a fixed time as in Figure 9. In all cases the portions of the weak till strips corresponding to significant basal melt produced significant sliding (e.g.,  $\geq 100$  m/a) at some point in the 5000 year runs, but this snapshot at the final time shows that some streams are “off.” Note that in all runs the peak surface speed outside of the weak strips, namely the surface speed from the SIA, is approximately 60 m/a.

[80] The time evolution of the modeled flow must be illustrated in a different way. A highly averaged measure is the volume of the whole ice sheet. As shown in Figure 10 the volume decreases in every experiment. The rate of volume loss is most rapid in the first 500 model years because the high driving stresses in the initial state produce fast sliding into the ablation area. This fastest initial flow is self-limiting because the geometry changes to produce

lower driving stresses, and because cold ice is advected down into the stream regions, with the ultimate effect that the modeled basal melt rate decreases or even becomes negative (refreeze). The till yield stress generally increases as a result of these thermomechanical changes.

[81] Experiment P1 was continued to a 100 ka run at 10 km resolution. The volume time series is shown in Figure 11. The “leveling out” suggested in the 5 ka result is realized and an approximate steady state is achieved. There is sliding flow at speeds typical of real ice streams at every time during this longer run, as shown in Figures 12 and 13. Figures 12 and 13 show the spatial average of the vertically integrated horizontal velocity over the positive thickness, downstream portion of each weak strip. There is rapid flow at speeds in

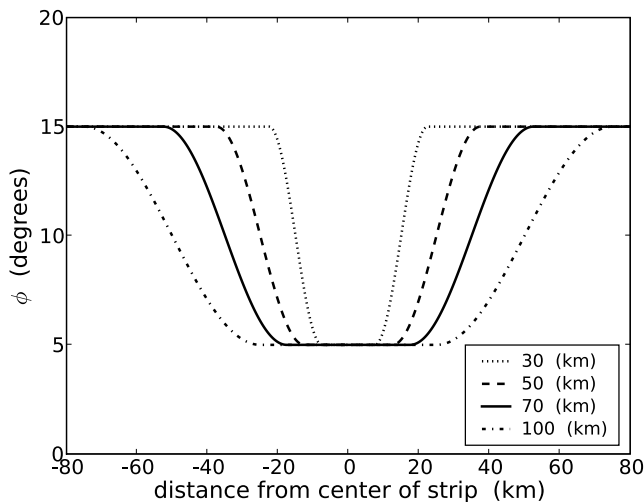


**Figure 7.** Till friction angle  $\phi$  across the four weak till strips in experiment P1, with given strip widths.

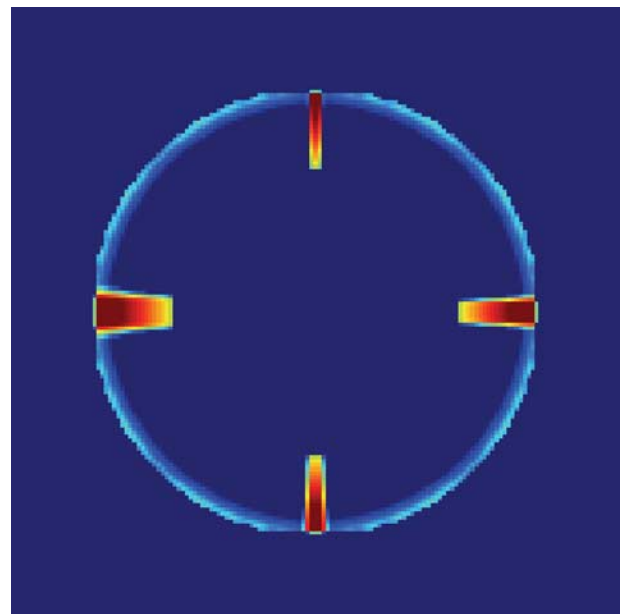


**Figure 8.** Difference  $\Delta\tau = \rho g H |\nabla h| - \tau_c$  between basal driving stress and till yield stress at start of experiment P1;  $\tau_c$  is computed from equation (19). Darkest red regions have  $\Delta\tau \geq 5 \times 10^4$  Pa, so they slide strongly when sliding is allowed.



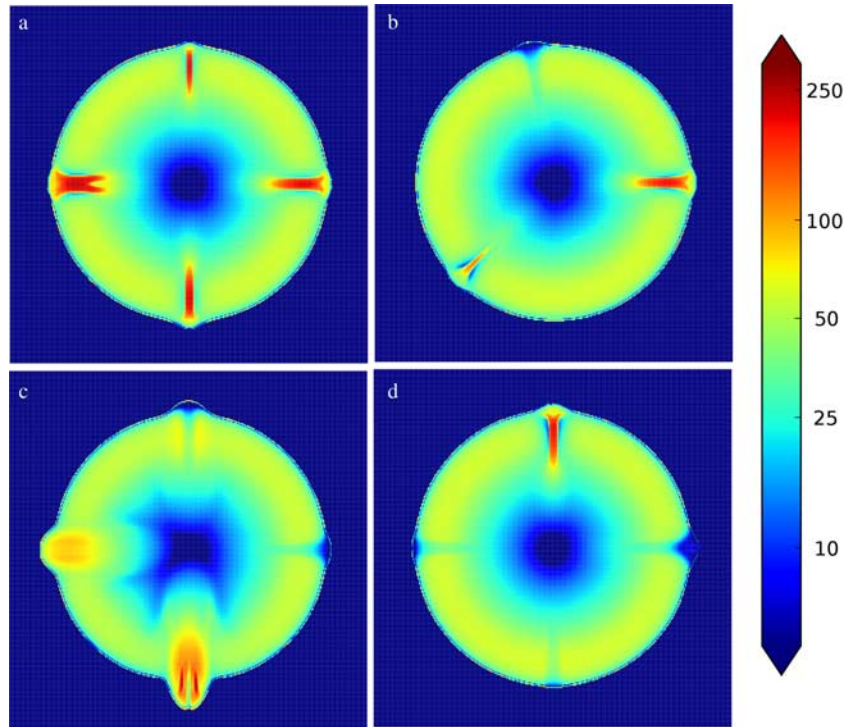


**Figure 9.** Modeled horizontal ice surface speed (m/a) in logarithmic color scale, at 5 km resolution and at the end of 5 ka runs: experiments (a) P1, (b) P2, (c) P3, and (d) P4.

excess of  $10^4$  m/a in the first few model years. Such high initial speeds are caused by the high driving stresses of the (nonsliding) initial state. The modeled flow clearly restabilizes to reasonable sliding speeds, but the 100 km wide stream in experiment P1 produces the most volatile flow. The explanation for this is that the center of the 100 km strip periodically cools and refreezes, causing shutdown of the central part of the sliding flow. Oscillations appear in the area-averaged flow speed, with period about 900 a (inset in Figure 13).

[82] Figures 12–17 which show flow speeds all include large and very brief excursions to much faster flow; these

are vertical lines sometimes going off scale. These correspond to discrete advance and retreat of the margin by a single or a few grid spaces. We believe that such discrete margin movement results in a brief reduction of back-pressure, followed by fast flow and advance of the margin to again “press” against the few essentially nonsliding ice-filled grid spaces at the margin and in the ablation area.

[83] We now show a sequence of Figures 14–19 from the highest-resolution (5 km) runs. Figure 14 shows that the two narrower streams in experiment P1 reach a level of relatively steady flow at average speeds of roughly 100 m/a within the first 1 ka. By contrast, the two wider streams

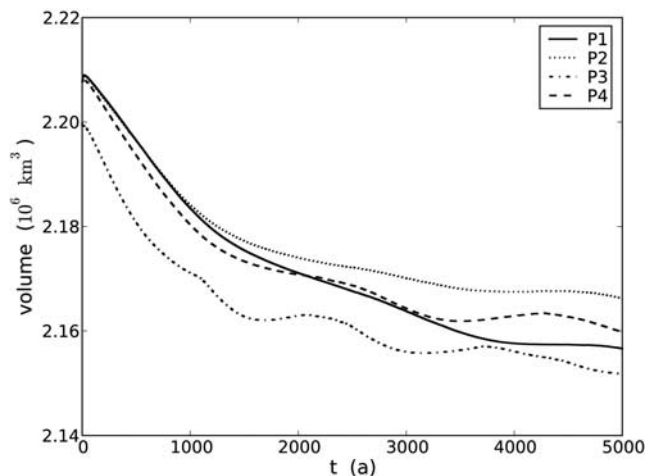


**Figure 10.** Modeled ice sheet volume for the four experiments at 5 km grid resolution.

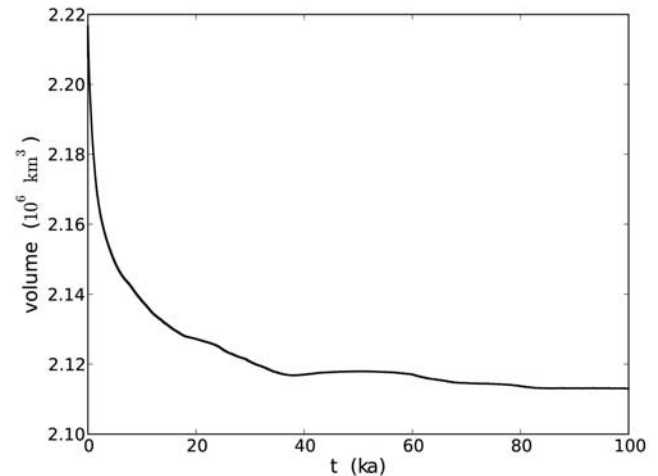


**Figure 11.** Modeled ice sheet volume for experiment P1 at 10 km grid resolution over a 100 ka span.

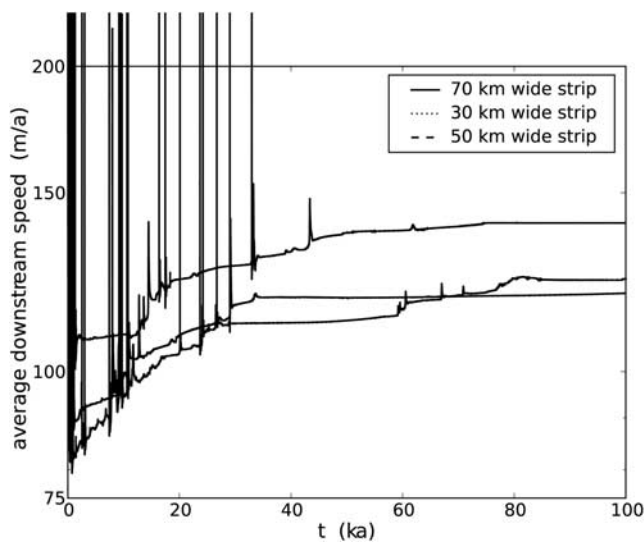


**Figure 12.** Average downstream speed for three of the four ice streams in experiment P1 over a 100 ka span.

enter cycles with average speeds varying from under 10 to over 100 m/a.

[84] Recall that experiment P2 examines how the flow depends on the grid orientation of weak strips, relative to the cartesian grid directions. As shown in Figure 15, although the strength and width of the weak strips are the same, the resulting speeds are somewhat different. There is rough agreement for the first 500 model years. The range of speed variation (20–200 m/a) roughly agrees for the whole 5000 years. All three streams enter similar oscillating states, but the cycles are out of phase and differ in period (1300 to 2100 years). Note that because all three streams are modeled within the same ice sheet there is some “competition” for ice near the divide (dome). Nonetheless grid orientation has some effect on flow speed in this experiment, a result which needs to be clarified in future work.

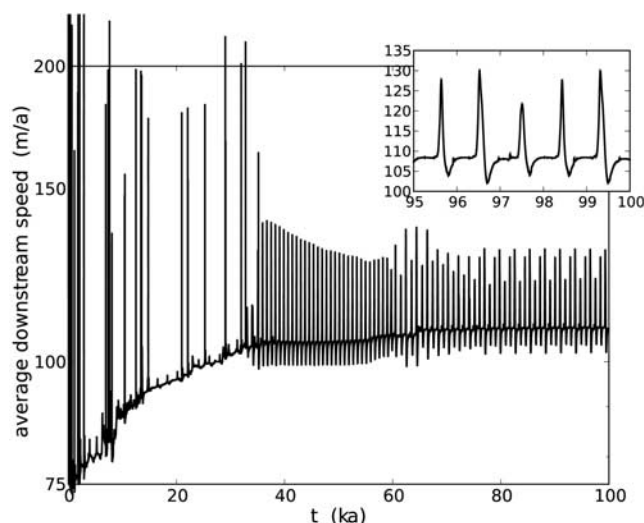


**Figure 13.** Average downstream speed for the 100 km wide ice stream in experiment P1 over a 100 ka span. Inset shows final 5 ka of run.

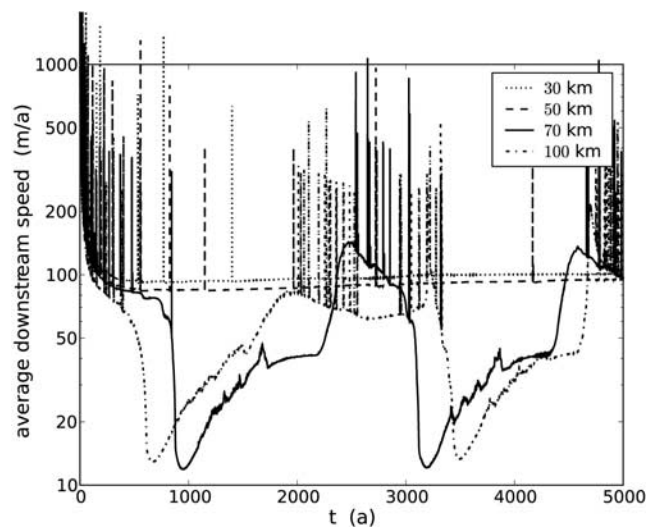


**Figure 14.** Average downstream speed for the ice streams in experiment P1 at 5 km resolution for a 5 ka run. Legend shows width of weak till strip.

[85] Experiment P3 evaluated the effect of bed slope on the modeled flow. We see in Figure 16 that larger slopes generate faster flow speeds and greater variability. The period of the cycle seems to be only weakly dependent on bed slope, however.

[86] Experiment P4 evaluated the effect of different choices for till friction angle in the downstream regions of the strips. Figure 17 shows that smaller till friction angle yields greater volatility in speed, with higher highs and lower lows. The variability of the modeled stream flow relates to the availability of basal water, which modulates till yield stress (section 2.7). Figure 18 shows the basal water thickness  $W$  at the end of the 5 ka run for P4. It should be compared to the P4 surface speed shown in Figure 9

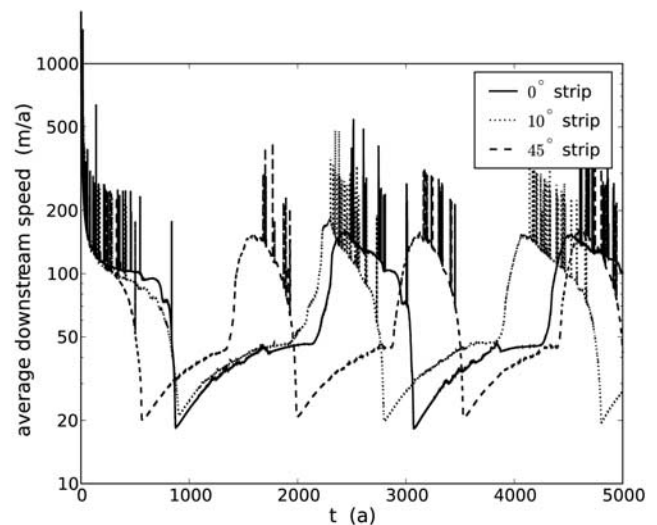


**Figure 15.** Average downstream speed for the three ice streams in experiment P2 at 5 km resolution. Legend shows weak till strip orientation relative to the closest grid (cardinal) direction.

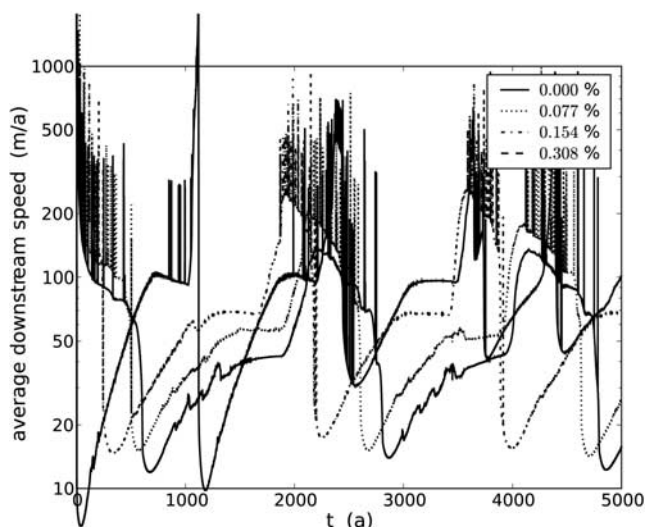


**Figure 16.** Average downstream speed for the ice streams in experiment P3 at 5 km resolution. Legend shows trough (bed) slope.

which shows only one active ice stream. The only active stream is the one which is underlain by the maximal amount of basal water ( $W = 2$  m), which is therefore the stream with the lowest till yield stress. Though the yield stress is lowest in the active stream, the till friction angle is slightly larger in the active stream ( $3^\circ$ ) than in the stream with the lowest friction angle ( $2^\circ$ ).

[87] Like Figure 9, Figure 19 also shows surface speed for experiment P4, but very near the beginning of the run (at 5 a). We see rapid sliding as the sheet reduces its driving stress to match the (recently and suddenly) reduced basal resistance which occurs at the start of all our experiments. In fact we see that the fastest flow at this time is in excess of 3000 m/a, and the weakest till corresponds directly to the lowest till friction angle because basal water thickness has

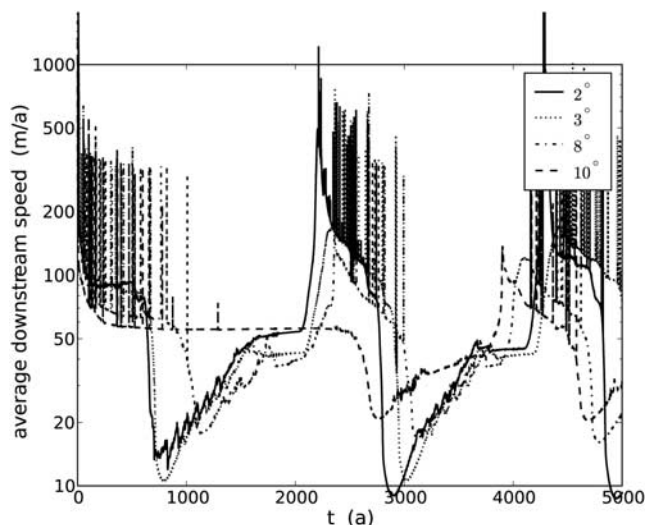


**Figure 17.** Average downstream speed for the ice streams in experiment P4 at 5 km resolution. Legend shows downstream till friction angle.

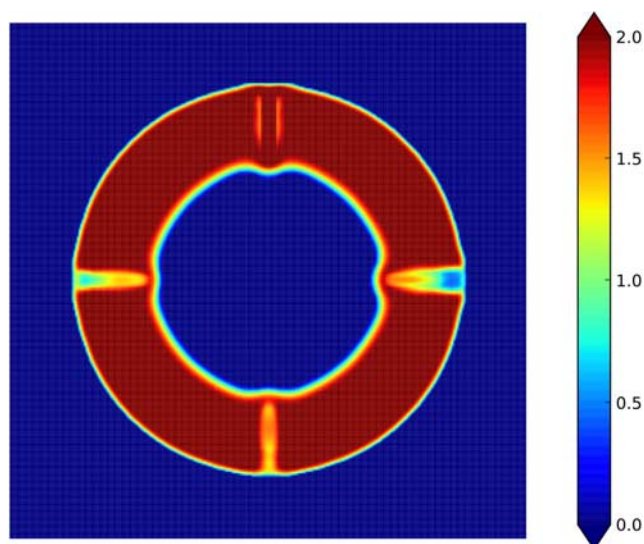


**Figure 18.** Modeled basal water effective thickness (m) at the end of experiment P4 at 5 km resolution.

not yet lost its approximate initial angular symmetry (Figure 5).

[88] The surface elevation evolves though the mass continuity equation in all runs. Because the sliding is rapid, surface evolution occurs rapidly and is mostly stabilized within the first 1 ka. Figure 20 illustrates the fact that the high driving stresses of the initial state have evolved, by the end of the 100 ka run, to lower driving stresses. There is roughly constant surface slope along the sliding portion of the stream. Compare Figure 2 of *Joughin et al.* [2001], which shows the surface profile along approximate flow-lines in the NE Greenland ice stream.

## 5.2. Time Steps and Effects of Grid Refinement

[89] Because the time stepping scheme is adaptive, incorporating stability conditions from multiple equations (subsection 3.3), the time step behavior is itself a significant

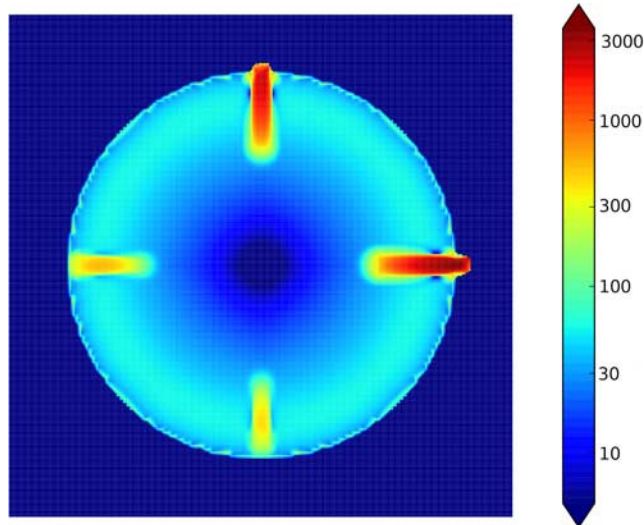


**Figure 19.** Modeled horizontal surface ice speed (m/a) from experiment P4 at 5 km resolution but at only 5 model years from onset of sliding.



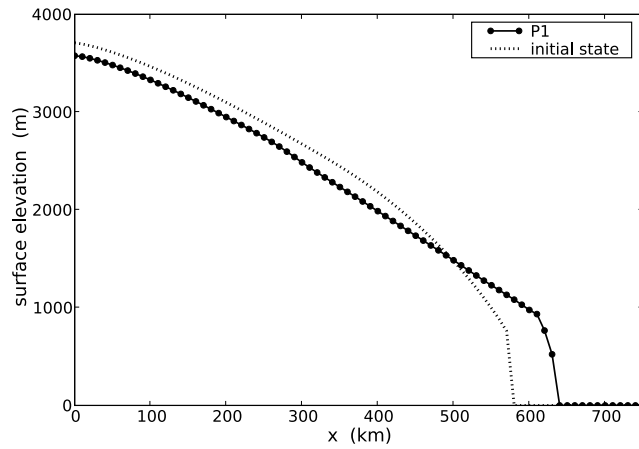


**Figure 20.** Surface elevation along the flow line corresponding to the center of the 70 km wide weak till strip in experiment P1 at 10 km resolution and at the end of a 100 ka run. Initial state before the onset of sliding also shown.

result. For the 5 km grid versions of all four experiments, the time step stabilized at about 0.1 model years. The time step became as small as 0.02 model years in the early period of transient fast sliding but in every case stabilized at the 0.1 model year level within 100 model years. For coarser grids the time step was larger, of course. Time step scaling essentially follows  $\Delta t \sim \Delta x^2$ , as expected from the explicit step condition for the diffusive SIA contribution to mass continuity.

[90] Figure 21 shows that experiment P1 behaves stably under changes in grid spacing when measured by volume. Over the full 5000 year evolution there is no obvious convergence toward a fine grid result. Evidence for convergence is seen when we consider only the first 1000 years of the run (Figure 22). In particular, the 7.5 and 5 km grid results remain very close for the first 500 years of the run. Grid refinement results for experiments P2, P3, and P4 are similar and are not shown.

[91] The 10 km grid experiments were repeated, with the vertical grid refined by a factor of two in the second

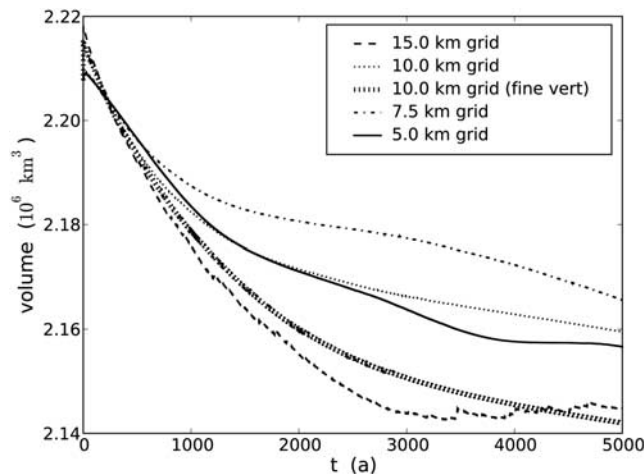


**Figure 21.** Effect of grid refinement on the volume time series for experiment P1.

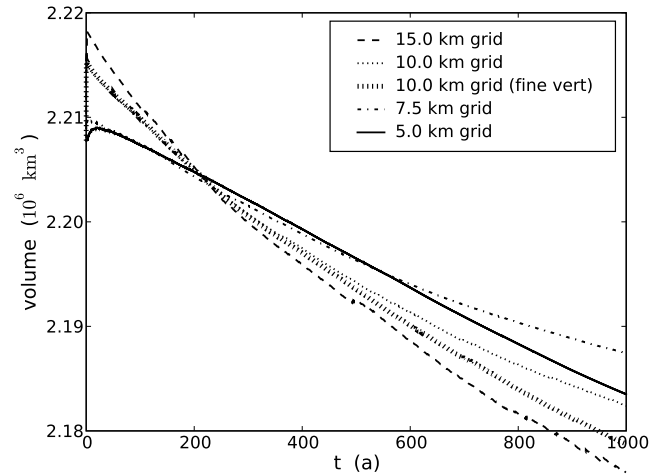


**Figure 22.** Effect of grid refinement on the volume time series in first 1 ka (experiment P1).

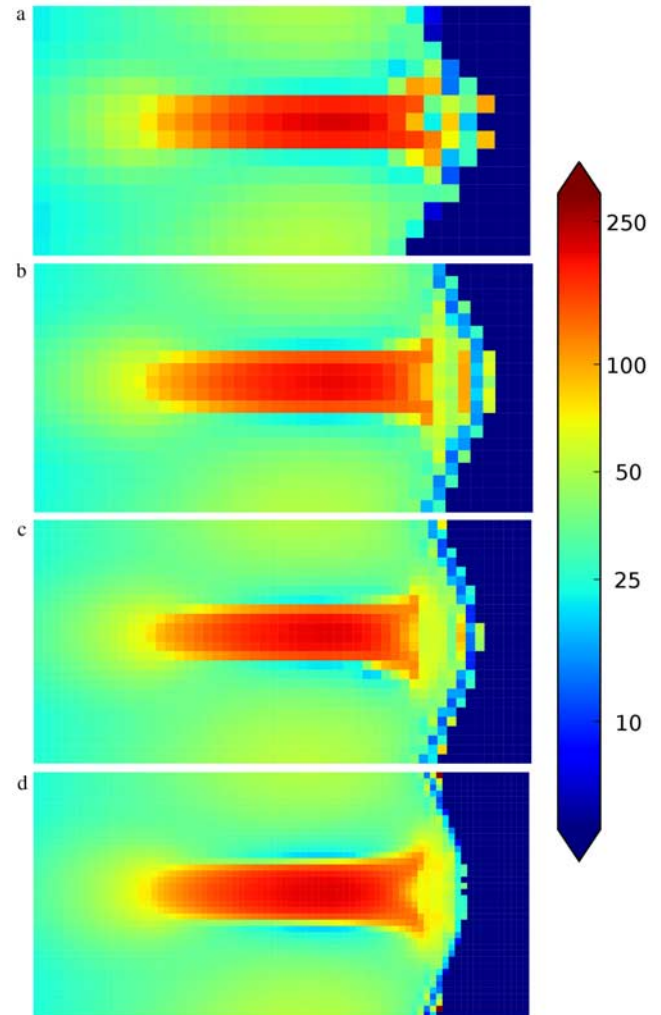


**Figure 23.** Detail of modeled horizontal surface ice speed (m/a) for experiment P1, in the same color scale used for Figure 9, at the end of 5 ka runs. Horizontal resolutions of (a) 15, (b) 10, (c) 7.5, and (d) 5 km.



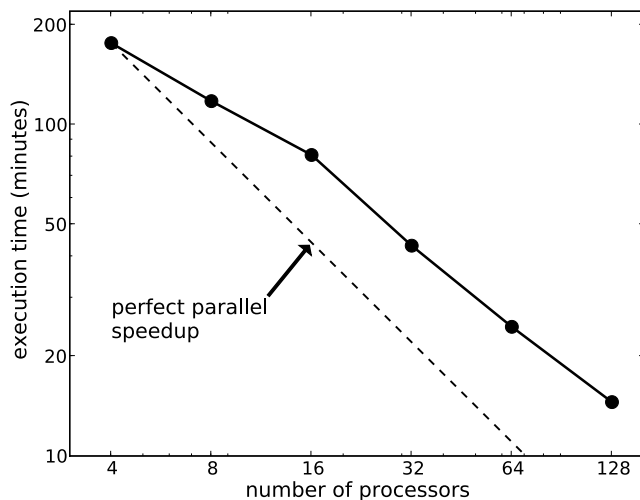


**Figure 24.** The wall clock time for experiment P1 decreases steadily with more processors.

instance. This case is labeled “fine vert” in Figures 21 and 22. This change in the vertical grid makes little difference in Figure 22. This suggests that the vertical grid choice, described above, is adequate. A theory explaining a preferred vertical grid refinement level is unknown to the authors.

[92] Grid refinement produces good behavior in terms of the spatial distribution of surface speed in modeled ice streams. Figure 23 shows the final state of the 70 km wide stream in experiment P1, at four horizontal grid spacings.

### 5.3. Parallelization

[93] In a parallel application like PISM, a doubling of the number of processors should halve the time to complete a run. Such simple scaling is never quite achieved in practice for parallel applications because of the time for interprocess communication and other “overhead.” In our case the parallel solution of linear systems is the most difficult part to speed up through parallelization, but this is handled in a sophisticated manner by the PETSc library [Balay et al., 2006]. See Appendix A. As shown in Figure 24, a perfect rate of speedup is not achieved but parallelization is notably effective anyway. The change to “asymptotically almost perfect” speedup in the range from 16 to 128 processors is likely an effect of memory parallelism, wherein the part of the simulation handled by a processor becomes small enough to fit in some level of cache memory.

## 6. Discussion

[94] The experiments above are for a simplified ice sheet with a steady and angularly symmetric climate (surface mass balance and temperature). On the other hand, new coupling mechanisms interact in a highly dynamic manner, as appropriate to real ice sheets. Thus results are not easily summarized, but we can list some common features:

[95] 1. All experiments start with a brief period of very fast sliding. In the initial state the driving stress is held fully by resistance at the base, but once sliding is allowed the driving stress is far out of balance. As shown in Figure 19, for example, the surface velocity exceeds 3000 m/a at 5 years

into experiment P4, but it later stabilizes to speeds typical of large ice streams with low slope (e.g., Figure 9).

[96] 2. After an initial period of rapid ice volume loss, caused by fast sliding into the ablation area, the ice sheet volume stabilizes. Fitting an exponential decay curve to the data shown in Figure 11 gives 22 ka as the exponential time for volume decay.

[97] 3. Surface velocity within ice streams sometimes enters a limit cycle. Wider ice streams are more likely to continue cycling because the center of the stream is the location at which advected cold ice can most easily cause basal refreeze. The basal refreeze process causes an increase in till yield strength and the (possibly temporary) cessation of sliding. In a wider stream there is more space for advection to dominate the energy balance, away from the additional dissipation heating at stream margins.

[98] 4. Experiments without a bedrock thermal layer (not shown) suggest that having a bedrock layer of modest thickness (e.g.,  $\geq 100$  m) is important. Without it the basal lubrication dynamics are more erratic. The need for a modest layer identified here, to mollify short timescale variations in basal lubrication, is distinct from the known importance of a deeper bedrock thermal layer for correctly assimilating long timescale climate variations into the (ice and bedrock) temperature field.

[99] 5. Schoof [2006a] observes that for the plastic till version of the SSA, the stability of time-dependent geometry evolution is unknown (as a mathematical matter). In fact there is no proof that cliffs will not appear on the ice surface at sliding/nonsliding transition locations in the Schoof [2006a] model, if it were to be used by itself in a time-dependent manner. Our model adds vertical plane shearing by the SIA, which causes the equation of mass continuity to be partly diffusive, which smooths the surface. It therefore exhibits stable geometry evolution.

[100] The fundamental explanation for the variability of stream flow in our experiments is exactly the mechanism described by Raymond [2000]. Namely, strain dissipation and friction heating compete with a combination of cold ice advection and basal drainage in providing lubrication for sliding. In our case, basal drainage is modeled only through limiting the basal water thickness to 2 m.

[101] The model in this paper is likely to be transitional, as even more complete ones become available. Many researchers are removing shallow assumptions and exploring better basal process models, for example. Directions for further parameter studies, and for model improvements, include these, which are listed in no principled order:

[102] 1. Experiments in this paper do not include floating ice shelves, which are subject to zero till yield stress and to the flotation criterion. On the other hand, the same PISM code for solving the SSA has successfully duplicated the EISMINT diagnostic comparison of modeled to observed Ross ice shelf velocities [MacAyeal, 1989].

[103] 2. Precise modeling of the flow of ice in the immediate vicinity of grounded margins and grounding lines requires both grid refinement and more complete stress balances than used here.

[104] 3. Detailed modeling of ice stream shear margins is also likely to require more complete stress balances than used here. Our model does allow transmission of side resistance into the interior of the sliding ice stream, but

only through membrane stresses. Better shear margin modeling might include bridging stresses, exotic concentration of strain dissipation heating and crevasse-related cooling [Truffer and Echelmeyer, 2003], anisotropy, and accumulation of damage in the ice fabric.

[105] 4. An important parameter dependence not explored in this paper is in the velocity combination scheme (subsection 2.8). The scheme involves a weighting function and a velocity scale for transition between flow types ( $f(|\mathbf{v}|)$  and 100 m/a, respectively, in equation (22)). These choices will be examined in future work. We will compare velocity results from this scheme to exact solutions of the Stokes equations and to numerical results from Stokes- and Blatter-type stress balance models.

[106] 5. The model for water thickness evolution and till strength in sections 2.4 and 2.7 might be improved by modeling additional processes. One could add the transport and the liquid dissipation heating terms in equation (5) of Clarke [2005], for example, or use the water conservation model by Johnson and Fastook [2002]. An alternative parameterization would track till void ratio, as in the undrained plastic till model of Tulaczyk *et al.* [2000b], instead of water thickness as here. The Tulaczyk *et al.* model should allow the removal of the artificial maximum for water thickness (2 m). It should also clarify the connection between basal melt rate and pore water pressure.

[107] 6. A front tracking [Greve, 1997a] or enthalpy gradient [Aschwanden and Blatter, 2009] polythermal model would improve the thermomechanical modeling generally and the basal melt model in section 2.4 in particular.

[108] 7. The heuristic concept that till is weaker at locations of lower bed elevation, because of a marine history for that bed [Huybrechts and de Wolde, 1999], can be directly implemented in our model.

[109] 8. Short timescale, local changes basal lubrication of the type associated with moulin drainage of surface melt [Zwally *et al.*, 2002] can be described in our model by forcing changes in pore water pressure.

## 7. Conclusion

[110] The ice dynamics model in this paper is capable of performing time-dependent, multimillennial simulations at whole ice sheet scale with a unified treatment of vertical shear stresses and membrane stresses. The treatment is “unified” in the sense that the flow type is not predetermined and can evolve from vertical-shear-dominated flow to membrane-stress-modulated sliding and back through well-behaved intermediate states. All equations are solved in parallel within the comprehensive, open source Parallel Ice Sheet Model (PISM), which allows high spatial resolution. It is a practical model for the dynamic response of ice sheets to climate change.

[111] The model combines two well-understood shallow approximations in a novel way, but some components of a complete (Stokes) stress balance are missing. On the other hand the model is of intermediate computational expense between easier thermomechanically coupled SIA models and more expensive higher-order and Stokes models. The experiments here include multiple simulations of the flow of a Greenland-scale ice sheet on a 5 km grid for a duration of 5000 model years. Many of the numerical and scientific

computing choices made here are an effective pathway toward parallel implementation at high resolution of the Blatter [1995] model with a plastic or power law basal resistance model [Schoof, 2009].

[112] The basal sliding velocity field generated by the model is continuous, unlike the sliding field generated by SIA models using a temperature-dependent sliding law [Payne *et al.*, 2000; Greve *et al.*, 2006]. Furthermore the underlying physical model for sliding used here is supported by observations [Clarke, 2005; Joughin *et al.*, 2004b; Raymond, 2000; Tulaczyk *et al.*, 2000a] and theory [Schoof, 2006a; Tulaczyk *et al.*, 2000b] for ice streams. The resulting flow speeds are realistic for those parts of ice sheets where bed gradients are modest, including the NE Greenland and Siple coast ice streams, for example.

## Appendix A: Finite Differences for SSA Stress Balance

[113] We use the notation of section 2.6, but let  $x = x_1$  and  $y = x_2$ . We denote an approximation of the function value  $f(x, y)$  at a grid point  $(x^i, y^j)$  by  $f^{i,j}$ . We use difference notation  $\delta_{+x}f^{i,j} = f^{i+1,j} - f^{i,j}$ ,  $\delta_{-x}f^{i,j} = f^{i,j} - f^{i-1,j}$ , and  $\Delta_x f^{i,j} = f^{i+1,j} - f^{i-1,j}$ , and corresponding notation for  $y$  differences. Temporarily denoting the product  $\bar{v}H$  by “ $N$ ”, our approximation of the first of equations (17) is

$$\begin{aligned}
 2 \frac{N^{i+\frac{1}{2},j}}{\Delta x} & \left[ 2 \frac{\delta_{+x}v_1^{i,j}}{\Delta x} + \frac{\Delta_y v_2^{i+1,j} + \Delta_y v_2^{i,j}}{4\Delta y} \right] \\
 & - 2 \frac{N^{i-\frac{1}{2},j}}{\Delta x} \left[ 2 \frac{\delta_{-x}v_1^{i,j}}{\Delta x} + \frac{\Delta_y v_2^{i,j} + \Delta_y v_2^{i-1,j}}{4\Delta y} \right] \\
 & + \frac{N^{i,j+\frac{1}{2}}}{\Delta y} \left[ \frac{\delta_{+y}v_1^{i,j}}{\Delta y} + \frac{\Delta_x v_2^{i,j+1} + \Delta_x v_2^{i,j}}{4\Delta x} \right] \\
 & - \frac{N^{i,j-\frac{1}{2}}}{\Delta y} \left[ \frac{\delta_{-y}v_1^{i,j}}{\Delta y} + \frac{\Delta_x v_2^{i,j} + \Delta_x v_2^{i,j-1}}{4\Delta x} \right] \\
 & + \tau_{b,1}^{i,j} = \rho g H^{i,j} \frac{\Delta_x h^{i,j}}{2\Delta x}. \tag{A1}
 \end{aligned}$$

The second of equations (17) is approximated by a similar scheme. In computing the staggered value of  $\bar{v}H$  the thickness  $H$  is averaged onto the staggered grid, while staggered grid values of the effective viscosity  $\bar{v}$  come from equation (14) using the same centered finite differences as in equation (A1). Figure A1 shows which of the quantities  $\bar{v}H$ ,  $v_1$ ,  $v_2$  are evaluated at which grid points in our scheme.

[114] To actually solve finite difference equation (A1) requires an “outer” nonlinear iteration and an “inner” linear iteration. The outer iteration produces a sequence of sparse linear problems in which the values of  $\bar{v}H$  are (temporarily) known. The inner iteration solves each linear problem for  $v_1$  and  $v_2$ .

[115] The outer iteration continues until successive values of  $\bar{v}H$  are within a specified tolerance. The criterion used for the results here is that the  $L^2$  norm of the difference of successive values of  $\bar{v}H$  is less than  $10^{-4}$  of the  $L^2$  norm of  $\bar{v}H$  itself. We do not require convergence of the velocities themselves in the outer iteration.

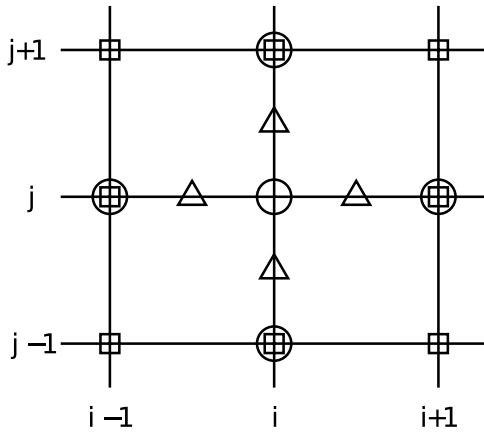


**Figure A1.** A stencil for finite difference scheme (A1) for approximating the first of equations (17). Triangles are staggered grid points where  $\bar{v}H$  is evaluated. Circles and squares show where  $v_1$  and  $v_2$ , respectively, are approximated.

[116] The inner linear problems can each be thought of as “ $A\mathbf{v} = \mathbf{b}$ ”, with the approximated driving stress  $\rho g H \nabla h$  as  $\mathbf{b}$ . Both the membrane stresses and the basal stress  $\tau_b$  appear on the left side as parts of the matrix  $A$ . We factor  $\tau_b$  into a coefficient times the velocity. The coefficient depends in a strongly nonlinear way on the velocity.

[117] If the grid has  $M_1 \times M_2$  horizontal points then there are  $2M_1M_2$  scalar unknowns. Using  $M_1 = M_2 = 301$  as in the 5 km grid results shown, each linear system has  $1.8 \times 10^5$  rows. Five grid values of  $v_1$  and eight grid values of  $v_2$  are involved in equation (A1), so there are 13 nonzero coefficients per row. These sparse linear problems are solved using a parallel iterative solver within PETSc [Balay et al., 2006]. For the results here we used the PETSc default, GMRES(30) with block Jacobi and ILU preconditioning [Saad, 2003]. This solver/preconditioner pair is one choice of many “Krylov” iterative methods within PETSc. (Which choices are optimal is, to our knowledge, open.) We use the default Krylov relative tolerance of  $10^{-5}$ .

## Appendix B: Traditional SIA Sliding Laws and Their Difficulties

[118] Sliding laws of the type used in EISMINT II experiment H [Payne et al., 2000] and ISMIP-HEINO [Greve et al., 2006] give the sliding velocity as a function of the driving stress. Ice colder than the pressure-melting temperature  $T_0^*$  does not slide.

[119] To analyze the difficulties of such sliding schemes, consider a slab on a slope of thickness  $H_0$  and slope  $\alpha$ . Use a horizontal coordinate  $x$  and a positive upward vertical coordinate  $z$ . Let  $u$  be the horizontal ice velocity,  $u_b$  the basal velocity, and  $T$  the temperature of the basal ice. Suppose that  $T$  increases along the flow, reaching pressure-melting temperature  $T_0^*$  at some location  $x_0$ , as shown in Figure B1. That is, suppose  $T < T_0^*$  for  $x < x_0$  while  $T = T_0^*$  for  $x > x_0$ . Finally, suppose  $u_b = 0$  when  $T < T_0^*$  and  $u_b = C\rho g H_0 \alpha$  when  $T = T_0^*$ , for a positive constant  $C$ . (We concretely choose a linear sliding law, but other power laws behave similarly.)

[120] The horizontal velocity within the ice is

$$u(x, z) = u_b(x) + \int_{b(x)}^z \frac{\partial u}{\partial z} d\zeta.$$

Recall that the SIA computes strain rate  $\partial u / \partial z$  from the ice temperature, surface slope, and depth below the surface. There is a jump in the basal velocity, so it follows that there is a jump in horizontal velocity at every vertical level  $z$  between the base and the surface of the ice

$$u(x_0^+, z) - u(x_0^-, z) = C\rho g H_0 \alpha. \quad (\text{B1})$$

[121] On the other hand, the ice is incompressible. Therefore the vertical velocity is formally infinite at all points in the ice column at  $x = x_0$ . Indeed, the vertical velocity is

$$w(x, z) = - \int_{b(x)}^z \frac{\partial u}{\partial x} d\zeta \quad (\text{B2})$$

anywhere the horizontal velocity is differentiable in  $x$ . In the ice column at  $x = x_0$  we necessarily interpret “ $\partial u / \partial x$ ” as infinity. (We have made harmless small-slope approximations, including assuming  $w = 0$  at the base of the ice.)

[122] It remains to be explained why this difficulty has not already required changes to ice sheet modeling practice. Consider a numerical scheme in which  $x_0$  is between a pair of gridpoints  $x^-$  and  $x^+$  which are separated by  $\Delta x$ . Suppose  $H_0 = 2000$  m,  $\alpha = 0.001$ ,  $\rho = 910$  kg m $^{-3}$ ,  $g = 9.81$  m s $^{-2}$ , and  $C = 10^{-3}$  m Pa $^{-1}$  a $^{-1}$  [cf. Payne et al., 2000]. Approximate

$$\frac{\partial u}{\partial x}(x_0, z) \approx \frac{u(x^+, z) - u(x^-, z)}{\Delta x}. \quad (\text{B3})$$

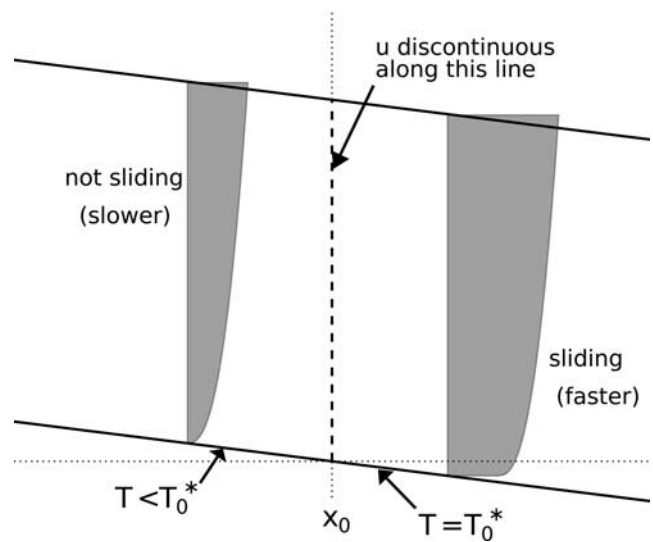


**Figure B1.** If the sliding law “turns on” where the basal ice reaches the pressure-melting temperature  $T_0^*$  then there is a discontinuity in the horizontal velocity in the whole ice column. The width of the grey band shows horizontal velocity  $u$ .



**Table B1.** Numerical Surface Value of the Vertical Velocity From Equations (B1)–(B3)

$\Delta x$ (km)	40	25	15	10	5	2	1
surface value of $w$ (m/a)	−0.9	−1.4	−2.4	−3.6	−7.1	−17.9	−35.7

Table B1 gives the resulting surface values of vertical velocity for values of  $\Delta x$  which might be used in ice sheet modeling. We see that for the rough grids ( $\sim 20$  km) used in EISMINT and ISMIP-HEINO, for example, this “infinity” is well hidden, unless the modeler carefully examines locations of slightly anomalous vertical velocities. The problem appears, however, on the finer grids which are necessary to resolve stresses in individual ice streams.

[123] Because the vertical velocity is a part of the energy conservation equation (7), anomalous vertical velocity is merely the start of unreasonable, time-dependent, thermomechanically coupled behavior. We hypothesize, for example, that the strange spokes in EISMINT II experiment H [Payne *et al.*, 2000] are a consequence of the mechanism described here. By contrast, the spokes for the nonsliding experiments in EISMINT II came from a different thermomechanical fluid instability mechanism, as discussed by Bueler *et al.* [2007, and references therein].

[124] We also believe that clear interpretation of the “Heinrich events” demonstrated in ISMIP-HEINO [Greve *et al.*, 2006] is confounded by consequences of thermomechanical coupling to this anomalous sliding mechanism. Of course it is reasonable to connect ice sheet sliding to Heinrich events, but continuum models for Heinrich events should include the membrane stresses which modulate sliding and control time-dependent ice stream behavior.

[125] **Acknowledgments.** NASA Cryospheric Sciences grant NAG5-11371 supported both authors. Comments by A. Aschwanden, two anonymous reviewers, and an attentive Associate Editor improved the paper substantially. We thank C. Khroulev, C. Lingle, D. Maxwell, S. Price, M. Truffer, and C. Schoof for help and essential correspondence. The Arctic Regional Supercomputer Center provided sufficient supercomputer time to allow us to recover from our mistakes, for which we are grateful.

## References

- Aschwanden, A., and H. Blatter (2009), Mathematical modeling and numerical simulation of polythermal glaciers, *J. Geophys. Res.*, **114**, F01027, doi:10.1029/2008JF001028.
- Balay, S., et al. (2006), PETSc users manual, revision 2.3.2 *Tech. Rep. Argonne Natl. Lab. 95/11*, Argonne Natl. Lab., Argonne, Ill.
- Blatter, H. (1995), Velocity and stress fields in grounded glaciers: A simple algorithm for including deviatoric stress gradients, *J. Glaciol.*, **41**(138), 333–344.
- Bueler, E., C. S. Lingle, J. A. Kallen-Brown, D. N. Covey, and L. N. Bowman (2005), Exact solutions and numerical verification for isothermal ice sheets, *J. Glaciol.*, **51**(173), 291–306.
- Bueler, E., J. Brown, and C. Lingle (2007), Exact solutions to the thermomechanically coupled shallow ice approximation: Effective tools for verification, *J. Glaciol.*, **53**(182), 499–516.
- Clarke, G. K. C. (2005), Subglacial processes, *Annu. Rev. Earth Planet. Sci.*, **33**, 247–276, doi:10.1146/annurev.earth.33.092203.122621.
- Fowler, A. C. (1997), *Mathematical Models in the Applied Sciences*, Cambridge Univ. Press, New York.
- Fowler, A. C. (2001), Modelling the flow of glaciers and ice sheets, in *Continuum Mechanics and Applications in Geophysics and the Environment*, edited by B. Straughan *et al.*, pp. 201–221, Springer, Berlin.
- Greve, R. (1997a), A continuum-mechanical formulation for shallow polythermal ice sheets, *Philos. Trans. R. Soc. London A*, **355**, 921–974.
- Greve, R. (1997b), Application of a polythermal three-dimensional ice sheet model to the Greenland ice sheet: Response to steady-state and transient climate scenarios, *J. Clim.*, **10**(5), 901–918.
- Greve, R. (2000), On the response of the Greenland ice sheet to greenhouse climate change, *Clim. Change*, **46**, 289–303.
- Greve, R., R. Takahama, and R. Calov (2006), Simulation of large-scale ice-sheet surges: The ISMIP-HEINO experiments, *Polar Meteorol. Glaciol.*, **20**, 1–15.
- Hindmarsh, R. C. A. (2004), A numerical comparison of approximations to the Stokes equations used in ice sheet and glacier modeling, *J. Geophys. Res.*, **109**, F01012, doi:10.1029/2003JF000065.
- Hindmarsh, R. C. A. (2006), The role of membrane-like stresses in determining the stability and sensitivity of the Antarctic ice sheets: Back pressure and grounding line motion, *Philos. Trans. R. Soc. London Ser. A*, **364**, 1733–1767, doi:10.1089/rsta.2006.1797.
- Howat, I. M., I. Joughin, and T. A. Scambos (2007), Rapid changes in ice discharge from Greenland outlet glaciers, *Science*, **315**(5818), 1559–1561, doi:10.1126/science.1138478.
- Hulbe, C. L., and D. R. MacAyeal (1999), A new numerical model of coupled inland ice sheet, ice stream, and ice shelf flow and its application to the West Antarctic Ice Sheet, *J. Geophys. Res.*, **104**(B11), 25,349–25,366.
- Hutter, K. (1983), *Theoretical Glaciology*, D. Reidel, Dordrecht, Netherlands.
- Huybrechts, P. (1990), A 3-D model for the Antarctic ice sheet: A sensitivity study on the glacial-interglacial contrast, *Clim. Dyn.*, **5**, 79–92.
- Huybrechts, P., and J. de Wolde (1999), The dynamic response of the Greenland and Antarctic ice sheets to multiple-century climatic warming, *J. Clim.*, **12**, 2169–2188.
- Jenssen, D. (1977), A three-dimensional polar ice-sheet model, *J. Glaciol.*, **18**, 373–389.
- Johnson, J., and J. L. Fastook (2002), Northern Hemisphere glaciation and its sensitivity to basal melt water, *Quat. Int.*, **95**, 65–74.
- Joughin, I., M. Fahnestock, S. Ekholm, and R. Kwok (1997), Balance velocities of the Greenland ice sheet, *Geophys. Res. Lett.*, **24**(23), 3045–3048.
- Joughin, I., M. Fahnestock, D. MacAyeal, J. L. Bamber, and P. Gogineni (2001), Observation and analysis of ice flow in the largest Greenland ice stream, *J. Geophys. Res.*, **106**(D24), 34,021–34,034.
- Joughin, I., W. Abdalati, and M. Fahnestock (2004a), Large fluctuations in speed on Greenland’s Jakobshavn Isbræe glacier, *Nature*, **432**(23), 608–610.
- Joughin, I., D. R. MacAyeal, and S. Tulaczyk (2004b), Basal shear stress of the Ross ice streams from control method inversions, *J. Geophys. Res.*, **109**, B09405, doi:10.1029/2003JB002960.
- MacAyeal, D. R. (1989), Large-scale ice flow over a viscous basal sediment: Theory and application to ice stream B, Antarctica, *J. Geophys. Res.*, **94**(B4), 4071–4087.
- MacAyeal, D. R., V. Rommelaere, P. Huybrechts, C. Hulbe, J. Determann, and C. Ritz (1996), An ice-shelf model test based on the Ross ice shelf, *Ann. Glaciol.*, **23**, 46–51.
- Mahaffy, M. W. (1976), A three-dimensional numerical model of ice sheets: Tests on the Barnes Ice Cap, Northwest Territories, *J. Geophys. Res.*, **81**(6), 1059–1066.
- Marshall, S. J., and G. K. C. Clarke (1997a), A continuum mixture model of ice stream thermomechanics in the Laurentide Ice Sheet: 1. Theory, *J. Geophys. Res.*, **102**(B9), 20,599–20,613.
- Marshall, S. J., and G. K. C. Clarke (1997b), A continuum mixture model of ice stream thermomechanics in the Laurentide Ice Sheet: 2. Application to the Hudson Strait Ice Stream, *J. Geophys. Res.*, **102**(B9), 20,615–20,637.
- Marshall, S. J., T. S. James, and G. K. C. Clarke (2002), North American Ice Sheet reconstructions at the Last Glacial Maximum, *Quat. Sci. Rev.*, **21**, 175–192.
- Morland, L. W. (1987), Unconfined ice-shelf flow, in *Dynamics of the West Antarctic Ice Sheet*, edited by C. J. van der Veen and J. Oerlemans, pp. 99–116, Kluwer Acad., Dordrecht, Netherlands.
- Morland, L. W., and I. R. Johnson (1980), Steady motion of ice sheets, *J. Glaciol.*, **25**(92), 229–246.
- Morton, K. W., and D. F. Mayers (2005), *Numerical Solutions of Partial Differential Equations: An Introduction*, 2nd ed., Cambridge Univ. Press, Cambridge, U. K.
- Paterson, W. S. B. (1994), *The Physics of Glaciers*, 3rd ed., Pergamon, Oxford, U. K.
- Paterson, W. S. B., and W. F. Budd (1982), Flow parameters for ice sheet modeling, *Cold Reg. Sci. Technol.*, **6**(2), 175–177.
- Pattyn, F. (2003), A new three-dimensional higher-order thermomechanical ice sheet model: Basic sensitivity, ice stream development, and ice flow across subglacial lakes, *J. Geophys. Res.*, **108**(B8), 2382, doi:10.1029/2002JB002329.



- Pattyn, F. (2008), Benchmark experiments for higher-order and full Stokes ice sheet models (ISMIP-HOM), *Cryosphere*, 2(1), 111–151. (Available at <http://www.the-cryosphere-discuss.net/2/111/2008/>.)
- Payne, A., et al. (2000), Results from the EISMINT model intercomparison: The effects of thermomechanical coupling, *J. Glaciol.*, 153, 227–238.
- Pollard, D., and R. M. DeConto (2008), A coupled ice-sheet/ice-shelf/sediment model applied to a marine-margin flowline: Forced and unforced variations, in *Glacial Sedimentary Processes and Products*, Int. Assoc. Sedimentol. Spec. Publ., 39, edited by M. Hambrey et al., Blackwell, Malden, Mass.
- Raymond, C. F. (2000), Energy balance of ice streams, *J. Glaciol.*, 46(155), 665–674.
- Ritz, C., A. Fabre, and A. Letréguilly (1997), Sensitivity of a Greenland ice sheet model to ice flow and ablation parameters: Consequences for the evolution through the last glacial cycle, *Clim. Dyn.*, 13(1), 11–24.
- Ritz, C., V. Rommelaere, and C. Dumas (2001), Modeling the evolution of Antarctic ice sheet over the last 420,000 years: Implications for altitude changes in the Vostok region, *J. Geophys. Res.*, 106(D23), 31,943–31,964.
- Saad, Y. (2003), *Iterative Methods for Sparse Linear Systems*, 2nd ed., Soc. for Ind. and Appl. Math., Philadelphia, Pa.
- Saito, F., and A. Abe-Ouchi (2005), Sensitivity of Greenland ice sheet simulation to the numerical procedure employed for ice-sheet dynamics, *Ann. Glaciol.*, 42(1), 331–336.
- Saito, F., A. Abe-Ouchi, and H. Blatter (2006), European Ice Sheet Modeling Initiative (EISMINT) model intercomparison experiments with first-order mechanics, *J. Geophys. Res.*, 111, F02012, doi:10.1029/2004JF000273.
- Saito, F., A. Abe-Ouchi, and H. Blatter (2007), An improved numerical scheme to compute horizontal gradients at the ice-sheet margin: its effect on the simulated ice thickness and temperature, *Ann. Glaciol.*, 46, 87–96.
- Schoof, C. (2004), On the mechanics of ice-stream shear margins, *J. Glaciol.*, 50(169), 208–218.
- Schoof, C. (2006a), A variational approach to ice stream flow, *J. Fluid Mech.*, 556, 227–251.
- Schoof, C. (2006b), Variational methods for glacier flow over plastic till, *J. Fluid Mech.*, 555, 299–320.
- Schoof, C. (2009), Coulomb friction and other sliding laws in a higher order glacier flow model, *Math. Models Methods Appl. Sci.*, in press.
- Shepherd, A., and D. Wingham (2007), Recent sea-level contributions of the Antarctic and Greenland ice sheets, *Science*, 315(5818), 1529–1532, doi:10.1126/science.1136776.
- Tarasov, L., and W. R. Peltier (2002), Greenland glacial history and local geodynamic consequences, *Geophys. J. Int.*, 150, 198–229.
- Truffer, M., and K. A. Echelmeyer (2003), Of isbrae and ice streams, *Ann. Glaciol.*, 36(1), 66–72.
- Truffer, M., and M. Fahnestock (2007), Rethinking ice sheet time scales, *Science*, 315(5818), 1508–1510, doi:10.1126/science.1140469.
- Tulaczyk, S., W. B. Kamb, and H. F. Engelhardt (2000a), Basal mechanics of Ice Stream B, west Antarctica: 1. Till mechanics, *J. Geophys. Res.*, 105(B1), 463–481.
- Tulaczyk, S., W. B. Kamb, and H. F. Engelhardt (2000b), Basal mechanics of Ice Stream B, west Antarctica: 2. Undrained plastic bed model, *J. Geophys. Res.*, 105(B1), 483–494.
- Vaughan, D. G., and R. Arthern (2007), Why is it hard to predict the future of ice sheets?, *Science*, 315(5818), 1503–1504, doi:10.1126/science.1141111.
- Weis, M., R. Greve, and K. Hutter (1999), Theory of shallow ice shelves, *Continuum Mech. Thermodyn.*, 11(1), 15–50.
- Wesseling, P. (2001), *Principles of Computational Fluid Dynamics*, Springer, Berlin.
- Zwally, H. J., W. Abdalati, T. Herring, K. Larson, J. Saba, and K. Steffen (2002), Surface melt-induced acceleration of Greenland ice-sheet flow, *Science*, 297(5579), 218–222, doi:10.1126/science.1072708.
- Zwinger, T., R. Greve, O. Gagliardini, T. Shiraiwa, and M. Lyly (2007), A full Stokes-flow thermo-mechanical model for firn and ice applied to the Gorshkov crater glacier, Kamchatka, *Ann. Glaciol.*, 45(1), 29–37.

J. Brown, Versuchsanstalt für Wasserbau, Hydrologie und Glaziologie, ETH Zurich, CH-8092 Zurich, Switzerland.

E. Bueler, Department of Mathematics and Statistics, University of Alaska Fairbanks, Box 756660, Fairbanks, AK 99775-6660, USA. (ffelb@uaf.edu)